



TURKISH JOURNAL OF TELECOMMUNICATIONS

A PUBLICATION OF TELECOMMUNICATIONS AUTHORITY

volume 1 number 2 2002
ISSN 1303-8702

TURKISH

JOURNAL OF
TELECOMMUNICATIONS



Published by Telecommunications Authority of the Republic of Turkey
(Telekomünikasyon Kurumu)

President : Ömer Arasıl

Department Supervisor : Güleser Aykara

Editor : İnan Güler

Secretarial Mediator : Süleyman Güngör

Designed : Cosmic Ajans

Printed : Pelin Ofset

Telekomünikasyon Kurumu

Basın ve Tüketiciler ile İlişkiler Müşavirliği

Yeşilırmak Sok. No: 16 Demirtepe/ ANKARA

Tel: 0 312 550 50 37 - 550 5307 Faks: 0 312 550 5246

e-posta: btm@tk.gov.tr Web: www.tk.gov.tr

TURKISH JOURNAL OF TELECOMMUNICATIONS

EDITOR
İnan GÜLER

ADVISORY BOARD

Ergül AKÇAKAYA
Işık University

Varol AKMAN
Bilkent University

Mustafa ALKAN
Telecommunications Authority

Mehmet ALTUNER
Telecommunications Authority

Mehmet BAYRAK
Selçuk University

Kenan DANIŞMAN
Erciyes University

Erdoğan DİLAVEROĞLU
Uludağ University

Numan DOĞAN
North Caroline University

Muhittin GÖKMEN
İstanbul Technical University

Adnan GÖRÜR
Niğde University

Kerim GÜNEY
Erciyes University

Emre HARMANCI
İstanbul Technical University

Ertuğrul KARAÇUHA
Telecommunications Authority

A.Hamdi KAYRAN
İstanbul Technical University

M.Kemal KIYMIK
Kahramanmaraş Sütçü İmam University

Hakan KUNTMAN
İstanbul Technical University

Mustafa MERDAN
Süleyman Demirel University

Avni MORGÜL
Boğaziçi University

Bülent ÖRENCİK
İstanbul Technical University

Erdal PANAYIRCI
Işık University

Bülent SANKUR
Boğaziçi University

Müzeyyen SARITAŞ
Gazi University

Hamit SERBEST
Çukurova University

Mete SEVERCAN
Middle East Technical University

Özgür ULUSOY
Bilkent University

B. Sıddık B. YARMAN
Işık University

Bingül YAZGAN
İstanbul Technical University

ISSN 1303 - 8702

VOLUME 1

NUMBER 2

IONOSPHERIC CLUTTER EFFECTS ON MONOSTATIC HF SURFACE WAVE RADAR SYSTEMS AND CLUTTER MITIGATION TECHNIQUES*

Bülent Şen, Burak Polat
TÜBİTAK Marmara Research Center , Information Technologies Research Institute,
P.O. Box 21, 41470, Gebze, Kocaeli
Tel: 90(262) 641 23 00 /4753 or 4822 Fax: 90 (262) 646 31 87
E-mail: bulents@btae.mam.gov.tr , polat@btae.mam.gov.tr

ABSTRACT

In this study, the reflected signal from the ionosphere in monostatic HF surface wave radar system is investigated in terms of atmospheric attenuation and Doppler spectral dispersion, by Chapman distribution and auto-correlation function when the process is stationary and time variant, respectively. The model-based analysis shows that doppler dispersion characteristics of the signal reflected from the ionosphere is not only highly dependent on zenith angle, radar operating frequency and turbulence velocity, but degrades the performance of the radar system as well. In order to improve the detection performance, clutter and interference mitigation techniques exploiting adaptive signal processing is reviewed with the incorporation of main and auxiliary antenna system overview.

Key Words: HF radar, ionosphere, electron number density, interference cancellation, adaptive processing.

MONOSTATİK YF YÜZEY DALGA RADAR SİSTEMİ'NDEKİ İYONOSFER KARGA ASI ETKİLERİ VE KARGAŞA BASTIRMA TEKNİKLERİ

ÖZET

Bu çalışmada, monostatik HF yüzey dalga radar sisteminin alıcısındaki sinyalin uğradığı atmosfer zayıflaması ve doppler izgesi dispersiyonu, atmosferdeki elektron yoğunluğunun durağan olduğu halde Chapman dağılımı ile, zamana bağlı olduğu halde ise özlenti işlevi ile modellenerek incelenmiştir. İyonosferden gelen sinyalin doppler izgesindeki davranışının güneşin Zenith açısı, radar çalışma frekansı, türbülans hızı gibi birçok parametreye bağlılığı irdelenmiş ve radar sistem ba arımına etkileri ortaya konmuştur. Radar sistem başarımını arttırmak için uyarlamalı sinyal işleme yordamları incelenmiş ve iyonosfer kargaşası ve girişim sinyallerinin bastırılması için ana ve yardımcı anten sistemleri gözden geçirilmiştir.

Anahtar Sözcükler: HF radar, İyonosfer, Elektron yoğunluğu, Girişim süzme teknikleri, Uyarlamalı işaret işleme

I. INTRODUCTION

In HF surface wave radars, while most of the energy is coupled to the surface of the earth, still some portion is radiated upwards and under certain conditions reflected back from the ionosphere. This reflected signal at the receiver is either multipath clutter or self interference. As far as the HFSWR is concerned, echoes from the ionosphere are unwanted signals. It is important that the HF surface wave radar system can distinguish these unwanted signals from the legitimate targets.

The detection performance of HF radar is mostly limited by external noise which can be divided into three categories as atmospheric, galactic and man-

made (CCIR, 1988). At the lower portion of the HF band (3-10 MHz), atmospheric noise usually dominates and the external noise level is 40-60 dB higher than thermal noise and subject to diurnal and seasonal variations as a result of temporal and spatial variations of atmospheric layers.

Doppler and multipath dispersion characteristics of ionospheric signal plays an important role in HF communication systems and has been investigated for decades in literature (cf. Davies, 1965). Multipath dispersion characteristics of ionospheric clutter in time domain have been extensively studied and verified with measurements by Bailey (1959) and Salaman (1962).

* This work is sponsored by Turkish Navy Research Center Command (ARMERKOM)

Time variant phase path of a signal which results from temporal characteristics of the ionosphere leads to a doppler spread distortion. Besides, phase path of the propagated signal through atmosphere depends on variations and dynamics of the total electron content (TEC) in troposphere and ionosphere. Spatial variation of TEC results from mostly solar radiation and partly cosmic rays. With sunrise, solar radiation starts to heat up the upper atmosphere and triggers the ion production which undoubtedly is the main source for multipath and doppler frequency dispersion. Thus, the position of the sun is the key factor in predicting the ionospheric clutter signal strength and its frequency spread in doppler spectrum.

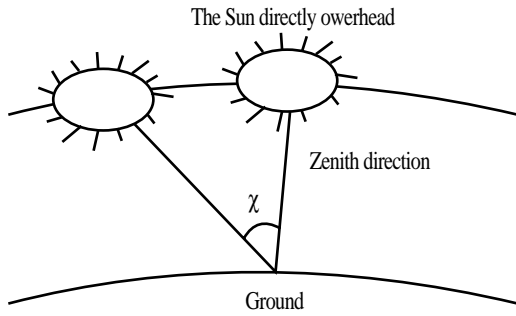


Fig. 1 Variation of zenith angle according to the position of the sun

In Figure 1, χ stands for the zenith angle of the sun and is defined as the angle between the sun and the zenith direction. In this study, a model is built up for investigating the impact of the ionospheric clutter on the HF surface wave radar system performance under the simplified restrictions given below:

- * Magnetic field effects are neglected,
- * The ionosphere is taken as a single and uniform layer,
- * The ionospheric clutter is assumed to originate from upward (overhead)
- * Zero refractivity is assumed in layer D.

II. STRUCTURE OF THE IONOSPHERE

For modelling the ionosphere, Chapman Layer model (Davies, 1965), which includes the dependence of both the zenith angle and height to TEC variation, is adopted. In this model the electron number density is given by

$$N(\chi, z) = N_Z \exp \left\{ \frac{1}{2} [1 - z - \sec(\chi) \exp(-z)] \right\} \quad (1)$$

where, $N[\text{m}^{-3}]$, electron number density, $N_0[\text{m}^{-3}]$, peak electron number density, χ [rad], zenith angle, H [m], scale factor, h [m], height, h_0 [m], height at which the peak electron number density occurs when the sun is directly overhead and $z = (h-h_0)/H$.

III. THE IONOSPHERIC MODEL

In the model the atmosphere comprises troposphere and ionosphere layers with refractivity profiles given below:

$$n(\vec{r}, f, t) = \begin{cases} n_T & , 0 \leq h \leq h_t \\ n_i(\vec{r}, f, t) = n_{i_0}(\vec{r}, f, t) + \Delta n_i(\vec{r}, f, t) & , h_t \leq h \leq h_i \end{cases} \quad (2)$$

IV. FORMULATION

The transmitted signal from a monostatic radar having a gaussian pulse shape with carrier angular frequency $\omega_0 (= 2\pi f_0 [\text{rad/sn}])$ can be expressed as

$$f(t) = A_0 \exp(-t^2 / 2\sigma^2) \exp[j(\omega_0 t + mt^2 / 2)] \quad (3)$$

In (3), A_0 is the signal amplitude, σ is the standard deviation in the gaussian distribution. The frequency sweep rate is taken as $m=0$ [rad/sn²] in the model.

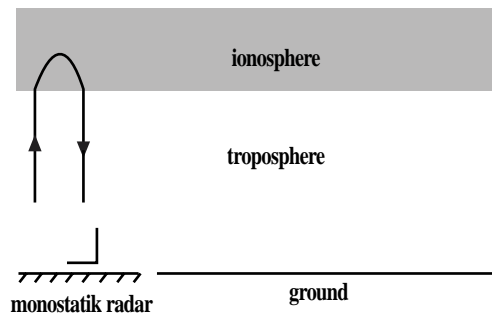


Fig. 2 Ray path of the HF radio signal

After reflecting back from the ionosphere, the time function of the received signal can be given as

$$F(t) = \frac{1}{2\pi} \int_{-\infty}^{\infty} f(\omega) \exp[-j\varphi(\omega)] \exp[j\omega t] d\omega \quad (4)$$

where $\exp[-j\varphi(\omega)]$ is the transfer function of the ionosphere (Millman et.al., 1971). $\varphi(\omega)$ is the frequency dependent phase shift introduced by the ionosphere which, for one way transmission path, is

$$\varphi(\omega) = \varphi_r(\omega) - j\varphi_i(\omega) = 2 \frac{\omega}{c} \int_0^R n ds \quad (5)$$

Replacing (5) into (4), the reflected signal can be rewritten as

$$F(t) = \frac{1}{2\pi} \int_{-\infty}^{\infty} f(\omega) \exp[-\varphi_i(\omega)] \exp[j\omega t] d\omega \quad (6)$$

Since $f(t)$ is gaussian with narrow bandwidth, the integral (6) can be approximated as

$$F(t) = \frac{1}{2\pi} \exp[-\varphi_i(\omega_0)] \int_{-\infty}^{\infty} f(\omega) \exp[-j\varphi_r(\omega)] \exp[j\omega t] d\omega \quad (7)$$

F can be evaluated to give (Millman et.al., 1971)

$$F(\tau) = \exp[-\varphi_i(\omega_0)] A_m \exp \left[j \frac{1}{2} \tan^{-1} \left(- \frac{\varphi_r''(\omega_0)}{\sigma^2 [1 + m\varphi_r''(\omega_0)]} \right) \right] \times \exp \left[j \left(\omega_0 \tau + \omega_0 \varphi_r'(\omega_0) + \frac{m\tau^2}{2} \right) \right] \exp \left[-\tau^2 / 2\sigma_m^2 \right] \quad (8)$$

where,

$$A_m = \frac{A_0}{[1 + m\varphi_r''(\omega_0)^2 + (\varphi_r'(\omega_0)/\sigma^2)^2]^{1/4}}, \sigma_m = \sigma \left[1 + m\varphi_r''(\omega_0)^2 + (\varphi_r'(\omega_0)/\sigma^2)^2 \right]^{1/2} \quad (9)$$

and $\tau = t - \varphi_r'(\omega_0)$.

$F(\tau)$ is the received signal when a gaussian signal is transmitted from the transmitter and reflected back from the ionosphere to the receiver. The signal shape in doppler spectrum can be obtained after a Fourier transformation is performed.

V. MODELING OF ELECTRON NUMBER DENSITY

The auto-correlation of electron number density variation between any two points in the ionosphere is defined as follows :

$$E \left[N(\vec{R}_1) N(\vec{R}_2) \right] = C(|\vec{R}_1 - \vec{R}_2|) \quad (10)$$

The well-known Gaussian distribution is selected for the mathematical expression of $C(r)$ auto-correlation function (Millman et. al., 1965)

$$C(r) = \sigma^2 \exp \left[-\pi r^2 / 4 \Lambda^2 \right], r \geq 0 \quad (11)$$

where $\sigma^2 = C(0)$ is the mean squared value of the refractive index fluctuation and $\Lambda [m]$ is the turbulence width. In the model, $N(h)$ stochastic process is obtained by using eigen decomposition of electron number density auto-correlation function.

VI. SIMULATION RESULTS

The flow diagram of the algorithm used in the model is depicted in Figure 3

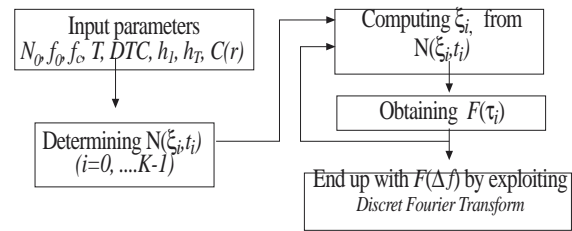


Fig. 3 Flow diagram of the algorithm

Where,

$\xi [m]$: Reflection point in the ionosphere,

$f_c [MHz]$: Critical frequency,

$T [sn]$: Pulsewidth,

$DTS [sn]$: Pulse repetition frequency,

K : Number of pulses transmitted within integration time

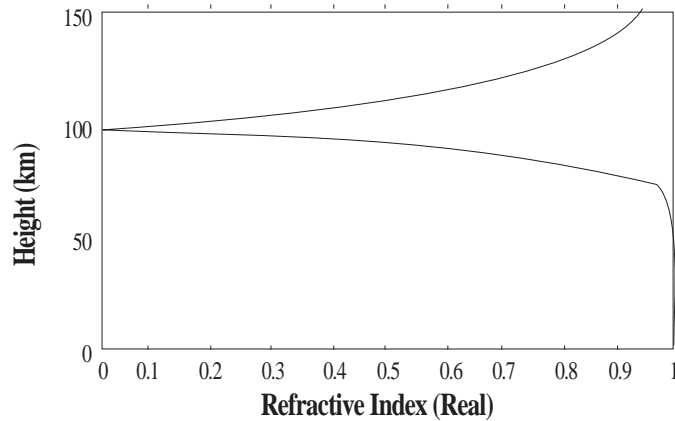


Fig. 4 Refractive index variation with height ($N_0=1.0062 \cdot 10^{12}$, $h_0 = 100$ km and $(\chi = 0^\circ)$)

Since the refractive index is taken as unity through D layer, transmitted signal is not subject to any refraction up to h_T . Any HF radio wave penetrating into the ionosphere undergoes a reflection at any point h_0 , ($h_T < h_0 < h_l$) where the real part of the complex refractive index ($n=n_r - jn_i$) goes down to zero (see Fig. 4). In order to establish an accurate

and realistic model, the parameters N_0 and h_0 in the Chapman Model need to be chosen such that the mathematical formulation reflects the actual physical phenomena given in Figure 4.

The dependence of the doppler frequency dispersion of the propagating signal to the turbulence velocity is depicted in Figure 5.

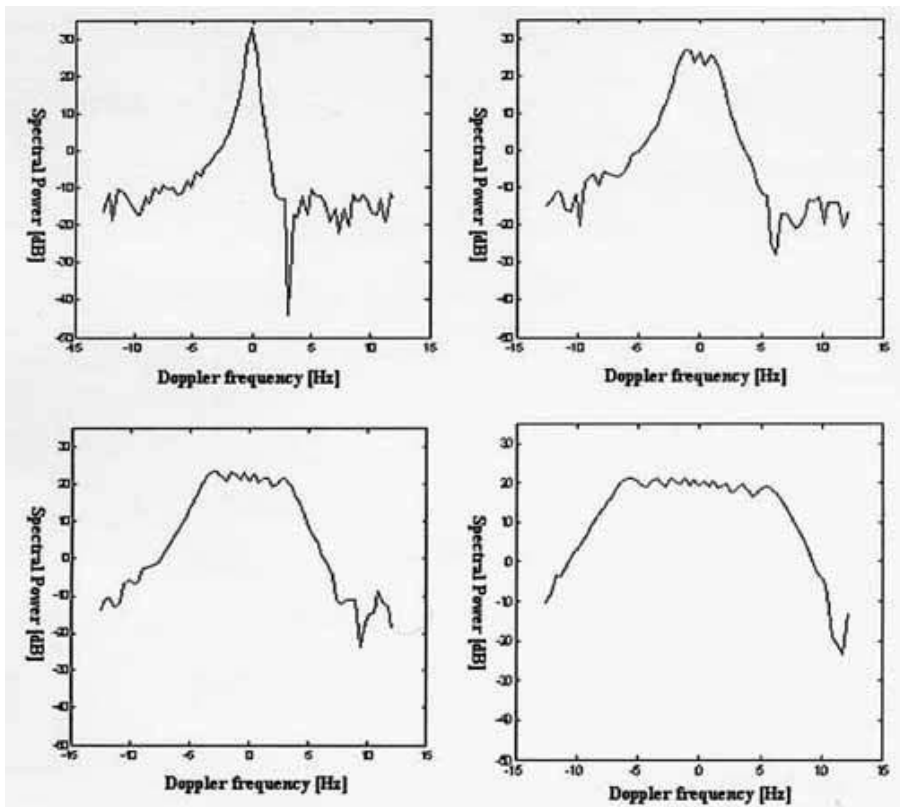


Fig. 5 Doppler dispersion of the received signal. $f_0 = 3$ MHz, turbulence velocity $v = 150, 300, 450, 600$ m/sn, turbulence width $tw = 200$ m, zenith angle $\chi = 0^\circ$

It is seen in figure 5 that at $\chi = 00$ the doppler distribution of the ionospheric clutter broadens with increasing turbulence velocity, while the spectral density decreases gradually.

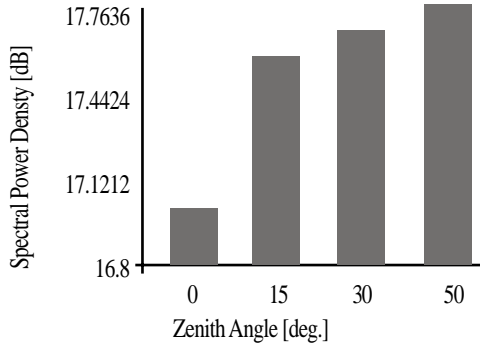


Fig. 6 Variation of the ionospheric clutter power density with the zenith angle

As seen in Figure 6, the spectral power density of the received signal from the ionosphere increases (atmospheric attenuation decreases) with increasing zenith angle. The empirical formulas in the literature [Davies, 1965] also meet with this fact and moreover, the probability of the degradation of the radar detection by ionospheric clutter increases.

Three methods can be deduced from the above investigations in order to minimize the severe effect of ionospheric clutter on radar system performance :

- * Take the measurements at the moment when the zenith angle approaches zero
- * Alter the operating frequency when the zenith angle is different from zero.
- * Predict the critical frequency at the time of the day and choose an operating frequency higher than the critical frequency ensuring no reflection from the ionosphere.

VII. IONOSPHERIC CLUTTER SUPPRESSION TECHNIQUES

The radar system performance is basically determined

by the characteristics of the radio frequency interference (RFI) source around the operating frequency. At HF band, the receiver system is purely external noise limited and the strength of the reflected signal from the target is sometimes very low compared to the external noise. The RFI is a random process and it is quite challenging to filter out the RFI component from the received signal.

In order to minimize the RFI signal or the clutter power, advanced signal processing techniques are employed among which are

- * Suppression techniques for clutter signal with known direction of arrival
- * Suppression techniques for clutter signal with unknown direction of arrival

In correspondence, there are two major clutter sources for HF surface wave radar operations : (Sevgi, et.al., 2001)

- * Ionospheric Clutter
- * Co-channel Interference

Ionospheric clutter is a signal with known direction of arrival (DOA) to the receiver, and created by upward radiation from the antenna to the ionosphere, caused mainly by antennas over poor ground and without a ground screen. For filtering this type of interfering signals, auxiliary antennas are widely used. As the ionospheric clutter is identical to the transmitted signal, auxiliary antennas need to be co-polarized (vertical polarization) with the main antenna system.

Co-channel interfering signal, which may have the same DOA, is one of the major problem for HF surface wave radar in 2-10 MHz frequency band. Ionospheric conditions at night time favor the propagation of radio signals over long distances (Leong, 2000). This increases the number of

interfering signals at a given radar site, making it sometimes impossible to find a clear channel to operate the radar. To suppress the co-channel interfering signal in the main signal, horizontal antennas orthogonal to that of the radar signal are used to capture the interfering signal, but not the vertically polarized radar signal. In practice, however, it is difficult to achieve a complete rejection of the radar signal at the outputs of the horizontal antennas which, in any case, gives better performance than vertically polarized auxiliary antennas.

Sky wave interfering signals like co-channel interference, are the type of signals with unknown DOA. There are two ways to filter out this type of interfering signals from the received signal :

* A passive monitoring system with the primary aim of finding clear channels for radar operation is used. After a quiet channel is captured, frequency agility is exploited to operate the radar in a more quiet frequency band for a robust and reliable detectability.

* Horizontal antennas with the aim of catching just the interfering signal are used incorporated with an adaptive signal processing method for cancellation.

Severe signal distortion may occur if the unwanted transmission is propagated through a highly perturbed ionosphere, as is commonly the case in the equatorial F region or the auroral zone. In these circumstances, the spatial characteristics of the received HF signals may exhibit significant temporal variability over the required coherent integration time (CIT). If the adaptive beamforming weights in the adaptive processor are held constant, it is obvious that this degrades the cancellation performance of the adaptive system as a result of temporal variations in the spatial structure of the interfering signals. Therefore, the adaptive weights need to be updated in certain intervals to tune the adaptive system to temporal variations and to achieve better adaptive processing performance.

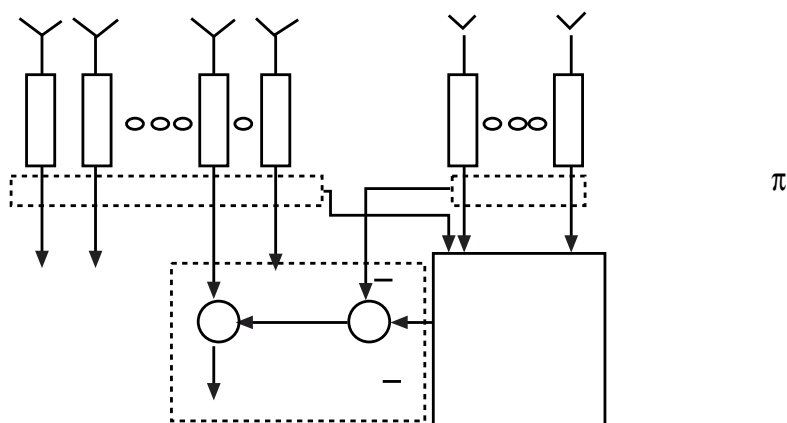


Fig. 6 Generic configuration of Side-Lobe cancellation system (Leong, 2000)

VIII. SIDELobe CANCELLATION TECHNIQUE

After the adaptive processing shown in Figure 6 for the target signals and the interfering signals from the same direction, the interference signal as well as the target signal is suppressed by around 25 dB which leads to a failure to detect targets close to the interference direction (Leong, 2000). This failure can be tackled if horizontal antennas auxiliary antennas are used.

In conclusion,

* For the target signal coming from the same direction as the interfering signal, both the interfering and the target signals are cancelled when the vertical antennas are used as auxiliary antennas. However, the target signal is preserved while the interference is cancelled when the horizontal antennas are used as they could not receive a portion of the target signal.

* Due to the fact that the interference components received by similar antennas are more correlated than those received by different antennas, the interference could be suppressed more substantially and interference plus noise floor could be lowered which leads to a better detection at receiver, when auxiliary vertical antennas are used. Thus, using vertical antennas when the target signal and interfering signal coming from different direction, outperform, leads to an enhancement in radar detection reliability.

IX. A SIMPLE TECHNIQUE ASSOCIATED WITH AN ANTENNA SYSTEM PROPOSAL FOR INTERFERENCE SUPPRESSION

One can introduce an antenna system for interference suppression with the following assumptions:

- * Target and interfering signals are coming from the same direction,
- * Transmitter and receiver antennas are left-handed circularly polarized,
- * Auxiliary antennas are right-handed circularly polarized.

This simple technique is outlined as follows :

$$X_m = R_m + I_m \tag{15}$$

$$X_a = R_a + I_a \tag{16}$$

Here,

R_m : Target signal at main antenna system receiver,

I_m : Interfering signal from the same direction as the target signal,

R_a : Target signal at auxiliary system receiver,

I_a : Interfering signal at auxiliary system receiver,

X_m : Total electric field expression at main antenna receiver end,

X_a : Total electric field expression at auxiliary antenna receiver end,

Mathematical expressions of R_m and I_m are:

$$R_m = \sqrt{2R_1^2} \left[\text{Cos } \gamma \cdot \vec{x} + \text{Sin } \gamma \cdot e^{j\frac{\pi}{2}} \cdot \vec{y} \right]$$

$$I_m = I_1 \cdot \vec{x} \quad (\text{left-handed, circular polarization}) \tag{17}$$

$$R_a = \sqrt{2R_1^2} \left[\text{Cos } \gamma \cdot \vec{x} + \text{Sin } \gamma \cdot e^{j\frac{\pi}{2}} \cdot \vec{y} \right]$$

$$I_a = I_1 \cdot \vec{x} \quad (\text{right-handed, circular polarization}) \tag{18}$$

In (17) and (18) γ stands for the angle between horizontal and vertical component of the total electric field

If I_m and I_a interfering signals have closer signal strength values, interfering signal component. will be filtered out by the technique, leaving only the target signal component at the receiver output.

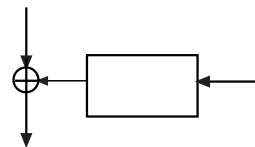


Fig. 7 Schematic diagram of interference suppression technique

Total electric field expressions at the main and auxiliary antenna receiver ends can be obtained from (17) and (18) as

$$X_m = \sqrt{2R_1^2} \left[\cos\gamma \cdot \bar{x} + \sin\gamma \cdot e^{j\frac{\pi}{2}} \cdot \bar{y} \right] + I_1 \cdot \bar{x} \quad (19)$$

$$X_a = \left[\sqrt{2R_1^2} \left[\cos\gamma \cdot \bar{x} + \sin\gamma \cdot e^{j\frac{\pi}{2}} \cdot \bar{y} \right] + I_1 \cdot \bar{x} \right] \cdot e^{j\pi} \quad (20)$$

$$X^* = X_m + X_a \quad (21)$$

$$X^* = 2 \sqrt{2R_1^2} \sin\gamma \cdot e^{j\frac{\pi}{2}} \cdot \bar{y} \quad (22)$$

It is seen from (22) that the amplitude of the output signal doubles the amplitude of the input of the main system receiver after the interfering signal is minimized (ideally filtered out). Signal strength is amplified while suppressing the interference.

In conclusion, if left and right-handed circular polarized antennas are used, the interfering signal

may be mitigated (ideally completely suppressed) and the signal strength is amplified as well.

X. CONCLUDING REMARKS

In this study, the generation of ionospheric clutter and its severe effects on the detection performance of monostatic HF surface wave radar system are investigated in association with clutter and interference mitigation techniques exploiting adaptive signal processing.

As a future work, the authors intend to introduce a more realistic ionospheric model by inserting measured TEC values in the expression of the refractivity profile in real time which complies with the temporal variation of the ionosphere. One should also try to reformulate the problem for alternate mathematical models of the ionosphere to include the anisotropic and stratified structure of the layer for a better understanding of radar propagation in the atmosphere.

REFERENCES

- Bailey D.K., (1959). The effect of multipath distortion on the choice of operating frequencies for high-frequency communication circuits, *IRE Trans. Antennas Propagat.*, vol AP-7, pp.397-404.
- Bello P.A., (1971). A study of the relationship between multipath distortion and wavenumber spectrum of refractive index in radio links, *Proc. IEEE*, vol 59, no.1, pp. 47-75.
- CCIR, (1988) Characteristics and Applications of Atmospheric Radio Noise Data, **CCIR Recommendation 322-3**,
- Davies K., (1965). *Ionospheric Radio Propagation*, Dover Publications, Inc., New York.
- Leong Hank W.H., (2000). A Comparison Of Sidelobe Cancellation Techniques Using Auxiliary Horizontal antennas and Vertical Antennas In HF Surface Wave Radar, *IEEE International Radar Conference*, pp. 672-677.
- Millman G.H., C.D. Bell, (1971). Ionospheric dispersion of an FM electromagnetic pulse, *IEEE Trans. Antennas and Propagat.*, vol 19, no.1, pp. 152-155.
- Salaman R.K., (1962). A new ionospheric multipath reduction factor (MRF), *IRE Trans. Commun. Syst. (Corresp.)*, vol CS-10, pp. 220-222.

DETERMINING ANTENNA FACTORS FOR EMC MEASUREMENTS

Bahattin Türetken Ali İhsan Yürekli Mehmet Yazıcı
TUBITAK-UEKAE P.O.Box 74 41470 Gebze, Kocaeli, Turkey
e-mail: bahattin@uekae.tubitak.gov.tr

ABSTRACT

In this study, a brief information on standard methods for determining antenna factors (AF) for electromagnetic compatibility (EMC) measurements is presented. Additionally, a new method of antenna factor measurement for 1m calibration has been introduced. Standard Site Method has been improved for obtaining 1m antenna factors at Open Area Test Site (OATS). Also antenna factor determination inside GTEM Cell is investigated. Calibrations with standard and alternative methods are performed and the reliability of these methods are discussed in the light of measurement results. Antenna factors of two UK National Physical Laboratory (NPL) calibrated antennas (biconic and small-size log periodic) are first determined on TÜBİTAK - UEKAE premises using standard methodology and results are compared. Antenna factors of biconic, log periodic and horn antennas have been obtained by using standart and alternative different methods. Resultant data are compared with original (NPL) and user (TÜBİTAK-UEKAE) data. A good agreement between the NPL measurement and TUBITAK-UEKAE measurement has been found.

Key Words: Antenna factor, Equivalent capacitance substitution, Standart site, Reference antenna, Electromagnetic compatibility

EMC ÖLÇÜMLERİ İÇİN ANTEN FAKTÖRLERİNİN BELİRLENMESİ

ÖZET

Bu çalışmada, elektromanyetik uyumluluk ölçümleri için anten faktörü belirlemede standart yöntemler hakkında kısa bir bilgi verilmiştir. Ayrıca, 1m kalibrasyonu için yeni bir yöntem önerilmiştir. Standart ve alternatif yöntemler kullanılarak ölçümler gerçekleştirilmiştir. Standart saha yöntemi, Açık Saha Test Alanı'nda (OATS) 1 m'lik anten faktörünü elde etmek için geliştirilmiştir. GTEM Hücresi içinde anten faktörü belirleme yöntemi de incelenmiştir. Standart ve alternatif yöntemlerle kalibrasyonlar gerçekleştirilmiş ve bu yöntemlerin güvenilirliği, ölçüm sonuçları ışığında tartışılmıştır. İngiltere NPL kalibreli iki antenin (bikonik ve log periyodik) anten faktörleri, TÜBİTAK-UEKAE EMC TEMPEST Test Merkezi tesislerinde belirlenmiş ve ölçüm sonuçları karşılaştırılmıştır. Bikonik ve log periyodik antenlere ek olarak bir adet horn antenin de anten faktörleri, standart ve alternatif yöntemler kullanılarak elde edilmiştir. Sonuç verileri, orijinal (NPL) ve kullanıcı (TÜBİTAK-UEKAE) verileriyle karşılaştırılmıştır. NPL ve TÜBİTAK-UEKAE ölçümü arasında uyumluluk gözlenmiştir.

Anahtar Sözcükler: Anten faktörü, E değeri kapasite yerine koyma metodu, Standart saha, Referans anten, Elektromanyetik uyumluluk

I- INTRODUCTION

Determining the antenna factor (AF) is a major step in making accurate field strength measurements for EMC compliance. There are well-established antenna calibration methods (ANSI C.63, 1998) to calculate these antenna factors at Open Area Test Sites (OATS). However, alternative methods utilizing different test setup and sites, like Gigahertz Transverse Electromagnetic (GTEM) Cell (Branough et.al, 1992; Türetken et.al, 2001) and Full Anechoic Chamber (FAC), (SAE ARP958, 1999) are also brought forth in recent years (Türetken et.al, 2002).

II- METHODS OF ANTENNA FACTOR DETERMINATION

Antennas and sensors play an important role in EMC compliance testing. The accuracy of calibration of these devices determines the accuracy of radiated emissions (RE) and radiated immunity (RI) test results.

Antenna calibration is the process of determining the numerical relationship, within an overall stated uncertainty, between the observed output of a measurement system and value, based on standard sources, of the physical quality being measured. The antenna factor (AF) is a ratio of measured E or H-field strength to the induced voltage delivered at the output of the antenna. AF must be highly accurate and the equipment used for measurement must be traceable to a national standard.

Antenna factors can be accurately obtained using different methods. These methods are: Standard Site Method (SSM), Reference Antenna Method (RAM) and Equivalent Capacitance Substitution Method (ECSM).

Some commonly used standards for determining antenna factors are given below:

- * Rod Antennas (9 kHz - 30 MHz)
 - SAE ARP 958 Rev D
 - ANSI C63.5-1998 (ECSM)
- * Biconical Antennas (30 - 300 MHz)
 - ANSI C63.5-1998 (SSM)
- * Log Periodic Antennas (300 - 1000MHz)
 - ANSI C63.5-1998 (SSM)
- * Horn Antennas (1 - 40 GHz)
 - SAE ARP 958 Rev D

II.1 Standard Site Method (30 MHz to 40 GHz)

The SSM for determining antenna factors (Smith, 1982) requires a standard antenna calibration site. The SSM requires three insertion loss measurements under identical geometries (antenna height, *h* and distance, *R*) using three different antennas taken in pairs, as shown in Fig. 1 Two measurement procedures may be used to determine insertion loss -a discrete frequency method and a swept frequency

method. For the discrete frequency method, specific frequencies are measured. At each frequency, the receive antenna is scanned over the height range given in the appropriate table to maximize the received signal. For the swept frequency method, measurements using broadband antennas may be made using automatic measuring equipment having a peak hold, storage capability, and tracking generator. In this method, both antenna height and frequency are scanned or swept over the required ranges, except for horn antennas, which are used at a fixed height of 2m.

The relation between insertion loss and antenna factor is given by

$$AF_1 + AF_2 = A_1 + 20\log(f) - 48.92 + E_D^{\max} \quad (1)$$

$$AF_1 + AF_3 = A_2 + 20\log(f) - 48.92 + E_D^{\max} \quad (2)$$

$$AF_2 + AF_3 = A_3 + 20\log(f) - 48.92 + E_D^{\max} \quad (3)$$

where, E_D^{\max} is the maximum received field at separation distance *R* from the transmitting antenna, $AF_{1,2,3}$ are the antenna factors of antennas 1,2 and 3 in dB(1/m), $A_{1,2,3}$ are the measured insertion losses in dB and *f* is the frequency in MHz. Solving equations (1), (2) and (3) simultaneously gives the expressions for the antenna factors in terms of the ground wave field strength term and measured insertion losses.

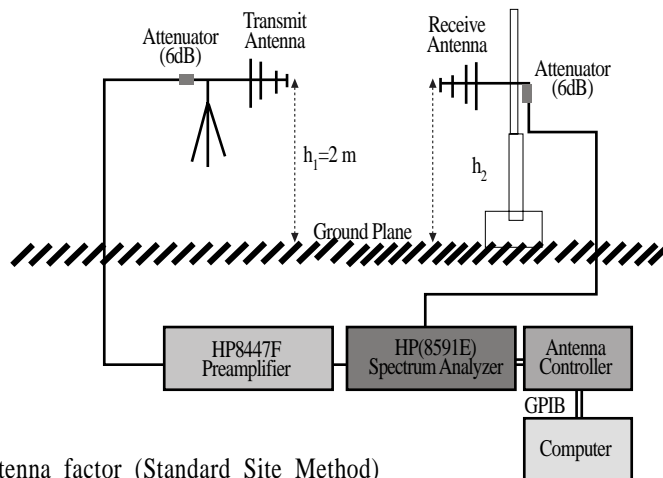


Fig. 1 Measurement of antenna factor (Standard Site Method)

II. 2 Reference Antenna Method (30 MHz to 1 GHz)

The Reference Antenna Method (RAM) provides a method of antenna calibration based on the use of a dipole with a well-matched balun (ANSI C.63, 1998).

II. 3 Equivalent Capacitance Substitution Method (9kHz to 30 MHz)

The Equivalent Capacitance Substitution Method (ECSM) shall be used to calibrate rod (monopole) antennas from 9 kHz to 30 MHz. The antenna factor in dB(1/m) is given by Equation (4) and the test setup is shown in Fig. 2.

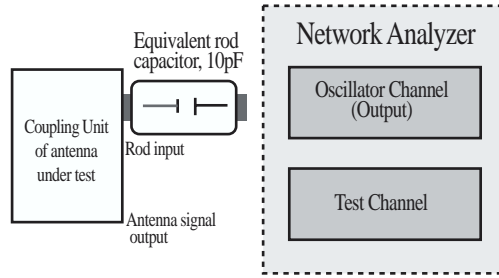


Fig. 2 Measurement of rod antenna factor

Antenna factor is calculated using,

$$AF = V_D - V_L + 6.02 \tag{4}$$

where,

V_D is the measured output of the signal generator in dB(uV)

V_L is the measured output of the coupler in dB(uV)

III. ANTENNA FACTOR DETERMINATION FOR 1 METER

Emissions measurements at 1m distance from the equipment under test (EUT) is called for in MIL-STD-461D, which stipulates that SAE ARP 958 procedure is to be followed for 1 m calibrations.

III. 1 SAE ARP 958

This method provides methods for determining antenna factors (AF) when measuring a source 1m away from the receive antenna in a shielded room versus a source at a greater distance (far field). AF of two identical antennas is given by;

$$AF = 20 \log_{10} \frac{9.73}{\lambda} - 10.98 + 10 \log_{10} (\lambda) - 10 \log_{10} \frac{V_R}{V_T} \tag{5}$$

where,

λ : wavelength in meters

V_R : voltage across the receive antenna terminals

V_T : voltage across the transmit antenna terminals

After some mathematical manipulations (1) can be reduced to,

$$AF = 8.7 - 10 \log_{10} (\lambda) - 10 \log_{10} \frac{V_R}{V_T} \tag{6}$$

III. 2 A New Implementation of ANSI C.63.5-1998

The basic setup is shown in Figure 1, keeping the distance between antennas as 1m . In this method both receive and transmit antennas (biconic or log periodic) are located 3m above the ground plane, in contrast to height requirements of the standard stated above. The area in which the setup is situated should be clear of obstructions to achieve a free-space environment. For 1m calibration where the ground reflection is anticipated to be non-existent or not to be picked up by the antenna being calibrated, E_D^{max} can be given by

$$E_D^{max} = 16.9 - 20 \log R, \text{ dB}(\mu V / m) \tag{7}$$

Substituting (7) into (1),(2) and (3) yields,

$$AF_1 = 8.7 - 10\log(\lambda) - \left\{ 10\log\left(\frac{V_{1R}}{V_{2T}}\right) + 10\log\left(\frac{V_{1R}}{V_{3T}}\right) - 10\log\left(\frac{V_{2R}}{V_{3T}}\right) \right\} \quad (8)$$

$$AF_2 = 8.7 - 10\log(\lambda) - \left\{ 10\log\left(\frac{V_{1R}}{V_{2T}}\right) + 10\log\left(\frac{V_{1R}}{V_{3T}}\right) - 10\log\left(\frac{V_{1R}}{V_{3T}}\right) \right\} \quad (9)$$

$$AF_3 = 8.7 - 10\log(\lambda) - \left\{ 10\log\left(\frac{V_{1R}}{V_{3T}}\right) + 10\log\left(\frac{V_{2R}}{V_{3T}}\right) - 10\log\left(\frac{V_{1R}}{V_{2T}}\right) \right\} \quad (10)$$

It is clear that the analytical expressions of two methods are approximately the same.

In order to compare the applicability of these methods, swept frequency method have been applied by means of a computer programme (Fig. 1). The results are given in Fig. 4 and Fig. 5.

IV. AN ALTERNATE METHOD OF DETERMINING ANTENNA FACTOR (GTEM CELL)

The method of calibration of an antenna inside a Gigahertz Transverse Electromagnetic (GTEM) Cell is placing the antenna at the center of the test volume, aligning the antenna such that the linearly polarized antenna is oriented vertically with the linearly polarized test volume and the floor of the GTEM Cell (see Fig. 3).

The field strength inside GTEM Cell is,

$$E = \frac{V_i}{h} \quad (11)$$

where,

E : Electric Field Strength (Volts/meter)

V_i : Input RF Voltage (Volts)

h : Septum Height (meter)

The definition of antenna factor is:

$$AF = 20\log\left(\frac{E}{V_0}\right) \quad (12)$$

where,

AF : Antenna Factor, (m^{-1})

V_0 : Antenna output voltage (Volts)

Combining (7) and (8) gives:

$$AF = 20\log(V_i) - 20\log(V_0) + 20\log(1/h) \quad (13)$$

A small log periodic antenna (Schwarzbeck 9108-217) was placed in the test volume of MEB GTEM 1750 and calibrated by using the test setup shown in Fig. 3 in the frequency range 300 MHz to 1 GHz.

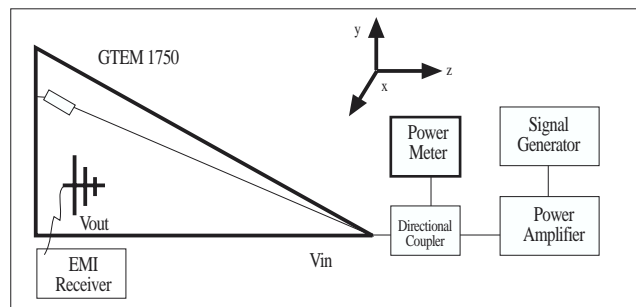


Fig. 3 Test Setup for Determining the Antenna Factor in a GTEM cell.

V. CONCLUSIONS

* Three biconical antennas covering the frequency range 30 MHz-300 MHz and three log periodic antennas covering frequency range 300 MHz-1000 MHz were calibrated by using standard-site method (Fig. 4 and Fig. 5).

* The requisite site attenuation measurements were made over 20mx17.3m metal ground plane. Site attenuation measurements were made using the swept frequency method described in (ANSI C.63.5, 1998).

* For accurate antenna calibration, the antenna separation distance R must be big enough to ensure that near-field effects and antenna-to-antenna mutual-coupling effects are negligible. To minimize antenna-to-ground plane mutual impedances and to ensure negligible contribution from the surface-wave component of the ground plane, the antenna heights must be big enough. For 1m antenna calibration SAE ARP 958 proposes the method of using two identical antennas in a shielded room. But the deficiencies of this method can be given as follows:

* The same antenna factor is assigned to two identical antennas.

* Discrete measurement method is used so that anomalies in the antenna factors readily apparent could be completely omitted with discrete measurements.

* A new implementation of ANSI C.63.5 has been introduced for one-meter antenna calibration. The antenna factors determined by this method are plotted in Fig. 5-8. Also shown are the NPL antenna factors measured by using SAE ARP 958 (1m) and ANSI C.63.5 (free space) methods. Generally, the results are very close to each other. Also the fluctuations on some frequencies on this method plotted in Fig 6-7 illustrate the advantage of using "swept" rather than "discrete-frequency" measurements.

* In Fig. 7 the antenna factors determined by using GTEM Cell have been compared with antenna factors obtained according to ANSI C.63.5 method (NPL and TUBITAK) and a very good agreement has been presented.

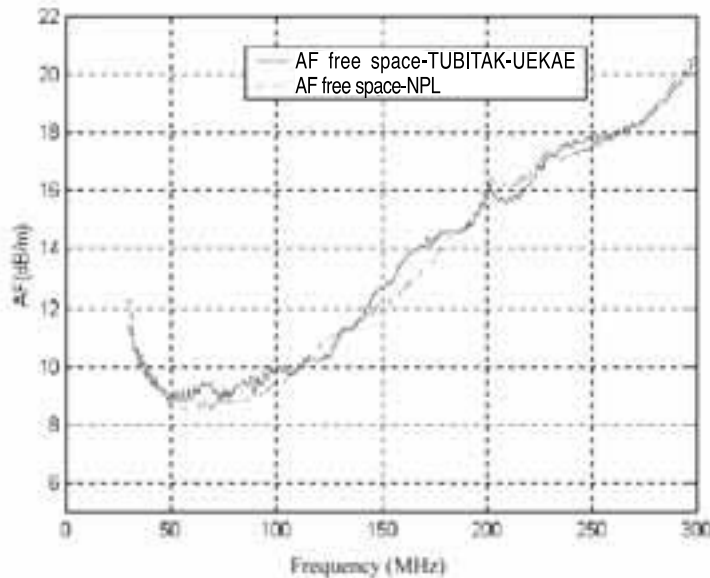


Fig. 4 Antenna Factor (dB/m)_free space - Biconical Antenna (Schwarzbeck BBA 9106)

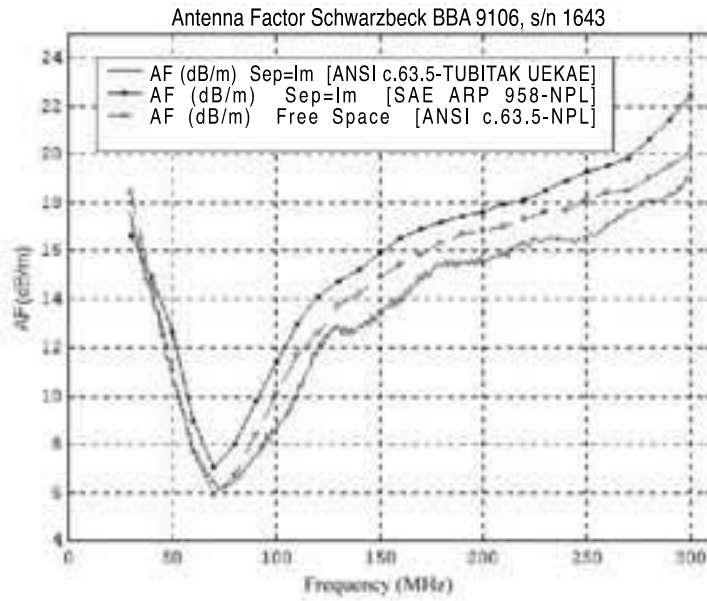


Fig. 5 Antenna Factor (dB/m)_free space - Log Periodic Antenna (SchwarzbeckUHALP 9108-A)

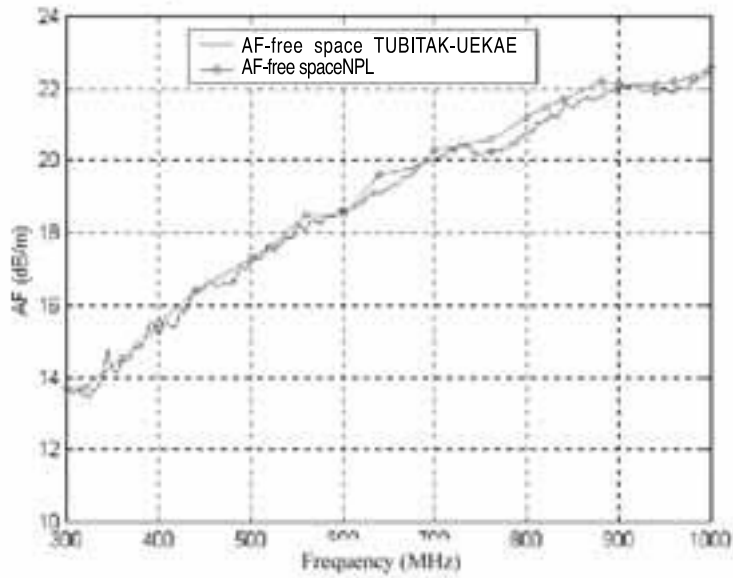


Fig. 6 Antenna Factor (dB/m) - Biconical Antenna (Schwarzbeck BBA 9106)

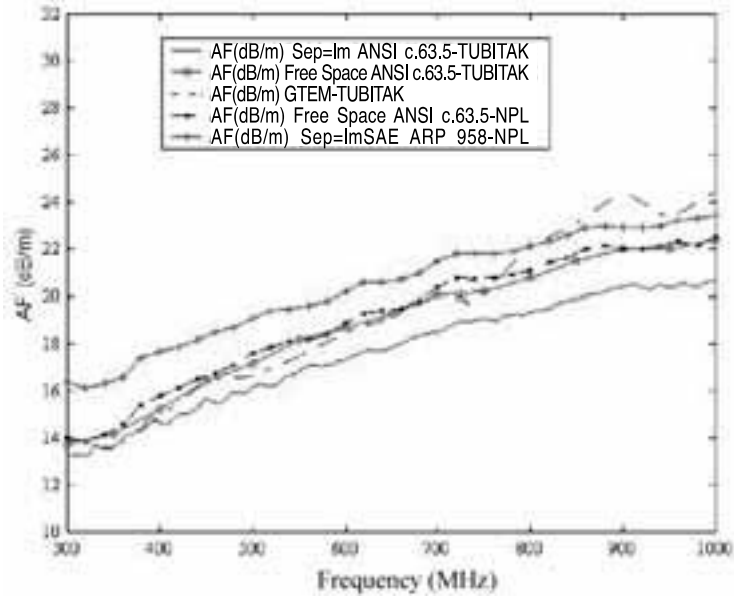


Fig. 7 Antenna Factor (dB/m) - Log Periodic Antenna (Schwarzbeck UHALP 9108-A)

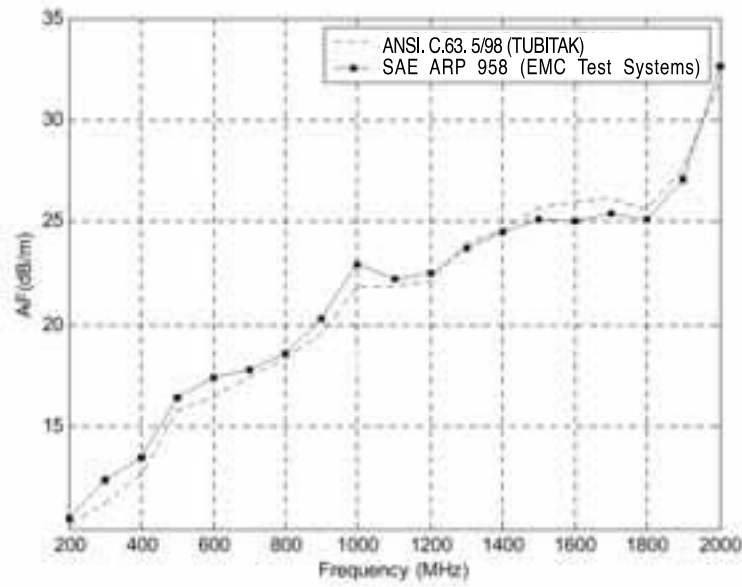


Fig. 8 Antenna Factor (dB/m) - Horn Antenna (EMCO-3106)

REFERENCES

- ANSI C63.5-1998, (1998). American National Standard for Electromagnetic Compatibility-Radiated Emission Measurements in Electromagnetic Interference (EMI) Control-Calibration of Antennas (9kHz-40 GHz).
- Bronaugh E.L., Osburn J.D.M., (1992). Measuring EMC Antenna Factors in the GHz Transverse Electromagnetic Cell, *IEEE 1992 International Symposium on EMC*, pp. 229-231, Anaheim, California A.B.D.
- SAE ARP 958, (1999). Electromagnetic Interference Measurement, Antennas, Standard Calibration Method.
- Smith, A.Jr., (1982). Standard-Site Method for Determining Antenna Factors, *IEEE Transactions on EMC*, vol. 24, no.3, pp. 316-322.
- Türetken B., Baran E., (2002). A New Implementation of ANSI C63.5 for 1 Meter Antenna Calibration, *URSI 27 th General Assembly 2002*, Maastricht, Holland.
- Türetken B., Yürekli A., (2001). Measuring EMC Antenna Factors: Comparison of Antenna Calibration Methods, *IV International Symposium on Electroamgnetic Compatibility and Electromagnetic Ecology*, pp. 316-319, St.Petersburg, Russia.

SEGMENTATION OF REMOTE-SENSING IMAGES BY THE GROW AND LEARN NETWORK

Tamer Ölmez, Zümray Dokur
Department of Electronics and Communication Engineering,
Istanbul Technical University, 80626 Maslak, Istanbul, Turkey
olmez@ehb.itu.edu.tr - zumray@ehb.itu.edu.tr

ABSTRACT

Abstract: In this study, a Grow and Learn (GAL) network is proposed for the segmentation of remote-sensing images. The seven images acquired by the Landsat-5 TM sensor are used to form the data set. Features are formed by the intensity of one pixel of each channel. Each feature represents the information of the same co-ordinate obtained from different channels. In this study, the GAL and the multi-layer perceptron (MLP) are comparatively examined for the segmentation of the remote-sensing images. The GAL and the MLP give 98% and 90% of classification performances, respectively. It is also observed that the training of the GAL takes less time compared to that of the MLP.

Key Words: Artificial neural network; Image segmentation; Remote sensing; Supervized learning.

BÜYÜ VE ÖĞREN AĞI İLE UZAKTAN ALGILANAN GÖRÜNTÜLERİN BÖLÜTLENMESİ

ÖZET

Bu çalışmada uzaktan algılanan görüntülerin sınıflandırılması için Büyü ve Öğren (GAL) ağının kullanılması önerilmektedir. Veri kümesi, Landsat-5 TM sensöründen elde edilen 7 görüntü kullanılarak oluşturulmuştur. Öznitelik vektörleri, kanallardan elde edilen benek gri seviyeleri kullanılarak oluşturulmaktadır. Herbir öznitelik, aynı koordinatta farklı kanallardan elde edilen bilgiyi temsil etmektedir. Bu çalışmada GAL ve çok katmanlı ağ, uzaktan algılama görüntülerin bölütlenmesinde karşılaştırmalı olarak incelenmektedir. GAL ve çok katmanlı ağ için sırasıyla %98 ve %90 sınıflama başarımları elde edilmiştir. Aynı zamanda GAL ağının çok katmanlı ağa göre daha hızlı eğitildiği gözlenmektedir.

Anahtar Sözcükler: Görüntü İşleme, Yapay Sinir Ağları, Uzaktan Algılanan Görüntülerin Bölütlenmesi

I. INTRODUCTION

The constitution of the right data space is a common problem in connection with classification. In order to construct realistic classifiers, the features that are sufficiently representative of the physical process must be searched. In the literature, it is observed that different transforms are used to extract desired information from remote-sensing images or biomedical images.

In the literature, it is observed that artificial neural networks are widely used for the segmentation of remote-sensing images (Berberoglu et al., 2000; Adam et al., 1998; Bruzzone et al., 1999; Giaconto et al., 2000; Serpico et al., 1996). Also, the combination of the neural networks and statistical algorithms is used for the segmentation of the remote-sensing images (Giaconto et al., 2000; Serpico et al., 1996). In most studies, single pixel intensity of each channel is used to determine the features. In some studies, features which contain textural measures (Berberoglu

et al., 2000; Olmo M.C. et al., 2000) are utilized. Image intensities at one or two neighborhood of the pixel (Dokur et al., 2000; Ölmez et al., 1996; Reza et al., 1991) and image intensities in multiple images (T1, T2 and proton density) (Qian et al., 1998; Vinitiski et al., 1997) are utilized to represent the tissues in magnetic resonance and computer tomography images. Wavelet transform (Qian et al., 1999), co-occurrence matrix (Haralick et al., 1973; Arrowsmith et al., 1999), Fourier transform (Feleppa et al., 1996) and spatial gray-level dependence matrices (Dasarathy et al., 1991) are used to extract textures in ultrasound images. Zhang et al. (Zhang et al., 1998) used wavelet transform for the detection of the micro-calcifications in digital mammograms.

Second-order statistical methods include gray-level co-occurrence matrices (GLCM) (Haralick et al., 1973) and gray-level run-length matrices (Dasarathy et al., 1991). Haralick (Haralick et al., 1973) proposed a set of 14 features calculated from a co-occurrence

matrix, whose elements represent estimates of the probability of transitions from one gray level to another in a given direction at a given inter-pixel distance. The features derived from GLCM include contrast, entropy, angular second moment, sum average, sum variance and measures of correlation. Parkkinen (Parkkinen et al., 1990) showed that GLCM can be applied on different inter-pixel distances to reveal periodicity in the texture. However, there is an inherent problem to choose the optimal inter-pixel distance in a given situation. Also, the GLCM method, in general, is not efficient since a new co-occurrence matrix needs to be calculated for every selected angle and inter-pixel distance. However, all these feature extraction methods increase the computational time of the classification process (Haering et al., 1999).

In the literature, it is observed that incremental neural network and competitive learning are widely used (Bruske et al., 1995; Fritzke et al., 1994; Fritzke et al., 1995). A number of approaches, advanced from self-organised map (SOM), have been proposed to achieve the objectives of retaining both the topology preserving and clustering properties. Fritzke (Fritzke et al., 1995) proposed a growing cell structure (GCS)

for self-organising clustering and topology preserving. To its simplicity, the competitive Hebbian rule has been used for topology learning in the Growing Neural Gas (GCS) (Fritzke et al., 1994) and Dynamic Cell Structure (Bruske et al., 1995). However, these algorithms add and delete nodes based on the 'resource' used in GCS. This has created some complexity in its implementation.

In this study, GAL network (Alpaydmn, 1990) is proposed as an incremental neural network to determine the nodes automatically, and to increase the classification performance. In order to decrease the overall computational time, feature vectors are formed simply by using pixel intensities.

II. METHODS

In this study, a data set is formed by using seven Landsat-5 TM images. Features are formed by the intensity of one pixel of each channel. Hence, the feature vector is formed by seven pixels' intensities. Each feature represents the information of the same co-ordinate obtained from different channels. Fig. 1 shows a sample representation of the pixel intensities used in the feature extraction method. In the feature extraction method, the neighborhood of

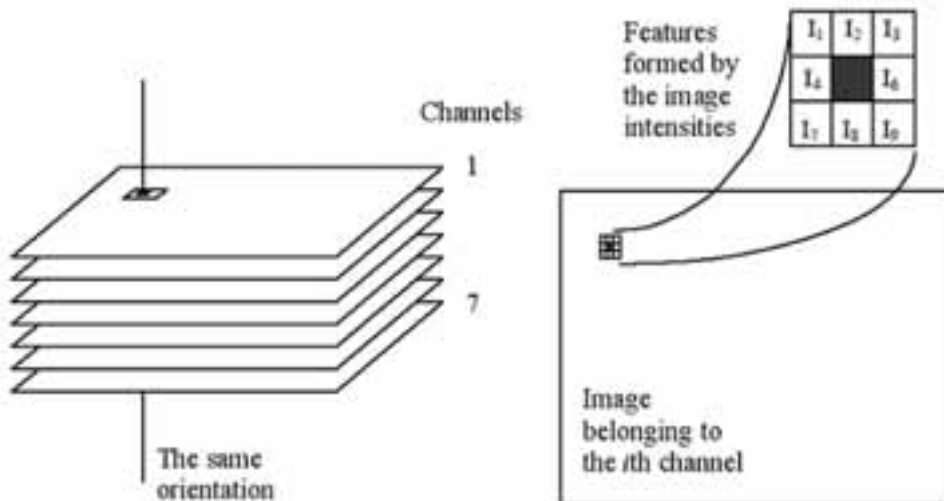


Fig. 1 The representation of the features. Black colour represents the central pixel (I_5), which is used alone to form the features. In the feature extraction method, the neighborhood of the central pixel is selected as zero.

the central pixel is selected as zero. Therefore, the dimension of the feature vector is 7. Since the features are represented by a simple method, computational times of the learning and classification processes are quite short.

After the feature extraction process, vectors are presented to artificial neural networks for the training. In the training of the GAL, the number of nodes of the network is automatically determined by its supervised learning scheme. A label is assigned to each output node. During the segmentation process, a feature vector is formed for each pixel and is presented to the GAL. The pixel under consideration is labelled by the label of the output node, which is nearest to the feature vector.

III. ARTIFICIAL NEURAL NETWORKS

The formulation of a proper data representation is a common problem in classification systems design. In order to construct realistic classifiers, the features that are sufficiently representative of the physical process must be found. If the right features are not chosen, classification performance will decrease. In this case, the solution of the problem is searched in the classifier structures, and artificial neural networks (ANNs) are used as classifiers to increase the classification performance.

There are four reasons to use an ANN as a classifier: (i) Weights representing the solution are found by iteratively training, (ii) ANN has a simple structure for physical implementation, (iii) ANN can easily map complex class distributions, and (iv) generalization property of the ANN produces appropriate results for the input vectors that are not present in the training set.

It is observed that the MLP is widely used in pattern recognition area. In this study, the GAL and the MLP are comparatively examined for the segmentation of remote-sensing images as both of them are trained by supervised learning schemes.

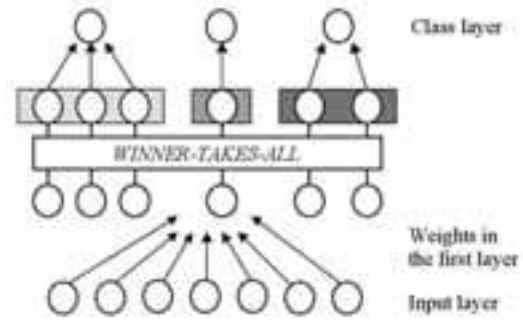


Fig. 2 Structure of the GAL network.

III.1. Gal Network

Fig. 2 shows the structure of the GAL network. The network grows when it learns category definitions. The network has a dynamic structure; nodes and their connections (weights) are added during learning when necessary. The basic advantage of GAL network is its fast learning.

The GAL network is an incremental network for supervised learning. The output nodes of the GAL network are formed by choosing vectors from the training set. All vectors in the training set have their own class labels. The procedure for the learning algorithm of the GAL network is as follows:

- Step 1. Initially choose a number of vectors randomly from the training set as many as the number of classes. Each vector represents only one class. Initialize each chosen vector as an output node of the GAL. Initialize the iteration number to zero value.
- Step 2. Increase the iteration number. If the iteration number is equal to the chosen maximum value, terminate the algorithm. Otherwise, go to step 3.
- Step 3. Choose one vector denoted by X randomly from the training set. Compute the distances between each output node of the GAL and the input vector, and find the minimum distance as follows:

$$d_0 = \sum_{j=1}^N (x_j - w_{oj})^2 \quad d_m = \min_0 (d_0) \tag{1}$$

where x_j is the j th element of the input vector X , w_{0j} is the j th element of the 0 th node of the GAL, and N is the present number of input nodes. Compare the classes of the input vector and the m th node nearest to the input vector. If their classes are the same, go to step 2. Otherwise go to step 4. Step 4. Include the input vector in the GAL network as a new output node. The elements of the input vector are assigned as the associated weights of the new output node of the GAL. Go to step 2. During the learning with GAL, nodes generated depend on the order of the input vectors. A node previously stored may become useless when another node nearer to the class boundary is generated. When a useless node is eliminated from the GAL network, the classification performance of the network does not change. In order to decrease the network size, these nodes are extracted from the GAL by the forgetting algorithm given below.

Step 1. Select the maximum iteration number as the number of output nodes in the GAL. Initialize the iteration number to zero.

Step 2. Increase the iteration number. If the iteration number is equal to the maximum value, terminate the algorithm. Otherwise, go to step 3.

Step 3. Choose the next node from the GAL in an order. This node is extracted from the network and is given as an input vector to the GAL network.

Step 4. Compute Eqs. (1). Compare the classes of the input vector and the m th node of the GAL. If their classes are not the same, go to step 5. Otherwise, go to step 3.

Step 5. Include the input vector again in the GAL. Go to step 2.

IV. COMPUTER SIMULATIONS

In this study, all the simulations are performed by using MATLAB 6.0. The seven images (each having a size of 256x256 pixels) acquired by the Landsat-5 TM sensor in an agricultural area in California are used for the data set. Fig. 3(a) shows the image corresponding to channel 1 (visible) of the TM sensor. Features are formed by the intensity of one pixel of each channel. Therefore, the dimension of the feature vector is 7. The pixels in the image are classified into seven classes by using the neural networks. The pixels are manually selected by a user to form the training set. The training set contains 7x10 feature vectors, 10 feature vectors belonging to each class. The test set also contains 7x10 vectors, which are different from the ones in the training set.

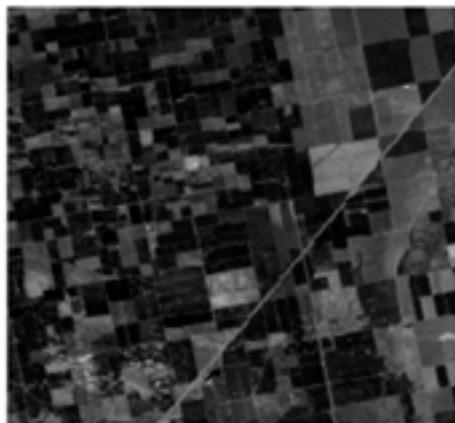


Fig. 3(a) The image corresponding to channel 1 (visible) of the TM sensor.



Fig 3(b) Segmentation result of the Kohonen network.

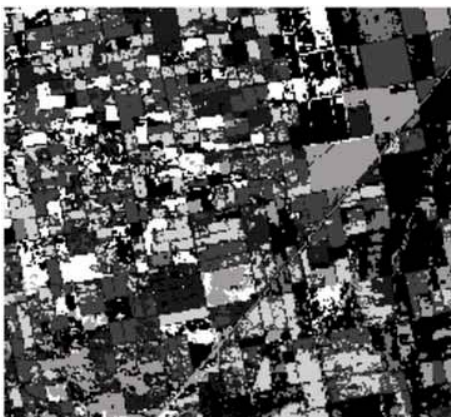


Fig. 3(c) Segmentation result of the GAL network.

The topology of the MLP is determined before the training. The structure of the MLP is found as 7-20-30-7 after ten trials. Fig. 3(a) is segmented into seven levels by using the MLP. Segmentation result is shown in Fig.3(b) The MLP gives 90% of classification performance for the test set. The number of nodes of the GAL is automatically determined during the training. The first layer of the GAL network consists of 10 nodes. The topology of the network is found as 7-10-7 by using the same training set. Fig. 3(a) is segmented into seven levels by using the GAL. Segmentation result is shown in Fig.3(c) The GAL network gives 98% of classification performance for the test set.

V. CONCLUSIONS

In this study, two neural networks with supervised

learning are compared for the segmentation of remote-sensing images. During the training of the GAL, the number of nodes of the network is determined automatically. However, the topology of the MLP must be estimated before the training. The determination of the optimal structure of the MLP takes a long time. It is observed that the training of the GAL takes less time compared to that of the MLP. Features are formed by the intensity of one pixel of each channel since the neighborhood of the central pixel is selected as zero. The intensity of a single pixel obtained from each channel does not contain any information about textures. The dimension of the feature vectors may be increased by selecting the neighborhood of the central pixel as one. Thus, feature vectors will contain textural information by this method. However, as the dimension of the feature vector grows, computational time increases proportionally.

The GAL and the MLP give 98% and 90% of classification performances for same testing set, respectively. It is observed that the supervised learning scheme of the MLP and GAL networks classifies pixels of remote-sensing image successfully. In a future study, features will be formed by the pixels at one neighborhood of the central pixel. The effect of the novel features on the classification performance will be examined.

REFERENCES

- Alpaydn E. (1990). Neural Models of Incremental Supervised and Unsupervised Learning, PhD. Thesis, *Ecole Polytechnique Federale De Lausanne*, Switzerland.
- Arrowsmith, M.J., Varley, M.R., Picton, P.D., Heys, J.D., (1999). Hybrid neural network system for texture analysis. *In: Seventh International Conference on Image Processing and its Applications*, Conf. Publ. no. 465, Vol. 1, pp. 339-343.
- Berberoglu, S., Lloyd, C.D., Atkinson, P.M., Curran, P.J., (2000). The integration of spectral and textural information using neural networks for land cover mapping in the Mediterranean. *Computer & Geosciences* 26, 385-396.
- Bruske, J., Sommer, G., (1995). Dynamic cell structure learns perfectly topology preserving map. *Neural Computation* 7 (4), 845-865.

- Bruzzone, L., Fernandez, D.P., (1999). An incremental-learning neural network for the classification of remote-sensing images. *Pattern Recognition Letters* 20, **1241-1248**.
- Dasarathy, B., Holter, E., (1991). Image characterization based on joint gray level run length distributions. *Pattern Recognition Letters*, **497-502**.
- Dokur, Z., Ölmez, T., (2000). Classification of magnetic resonance images using a novel neural network. In: *IEEE-EMBS Asia Pacific Conference on Biomedical Engineering*, Hangzhou, China.
- Feleppa, E.J., Kalisz, A., Melgar, J.B.S., Lizzi, F.L., Liu, T., Rosado, A.L., Shao, M.C., Fair, W.R., Wang, Y., Cookson, M.S., Reuter, V.E., Heston, W.D.W., (1996). Typing of prostate tissue by ultrasonic spectrum analysis. *IEEE Transactions on Ultrasonics, Ferroelectrics, and Frequency Control* 43(4), **609-619**.
- Fritzke, B., (1994). A growing neural gas network learns topology. In: Tesauro G., Touetzky D.S. and Leen T.K., *Advances in Neural Information Processing Systems*, Vol. 7, MIT Press, Cambridge, MA.
- Fritzke, B., (1995). Growing cell structure- A self-organizing network for unsupervised and supervised learning. *Neural Networks* 7 (9), **1441-1460**.
- Giacinto, G., Roli, F., Bruzzone, L., (2000). Combination of neural and statistical algorithms for supervised classification of remote-sensing images. *Pattern Recognition Letters* 21, **385-397**.
- Haering, N., Lobo, N.D., (1999). Features and classification methods to locate deciduous trees in images. *Computer Vision and Image Understanding* 75 (1-2), **133-149**.
- Haralick, R.M., Shanmugan, K., Dinstein, I., (1973). Texture feature for image classification, *IEEE Transactions on Systems, Man, and Cybernetics* 3, **610-621**.
- Jozwik, A., Serpico S., Roli, F., (1998). A parallel network of modified 1-NN and k-NN classifiers application to remote-sensing images classification. *Pattern Recognition Letters* 19, **57-62**.
- Kohonen, T., (1988). *Self-Organization and Associative Memory*. New York, Springer-Verlag.
- Kurnaz, M.N., Dokur, Z., Ölmez, T., (2001). Segmentation of ultrasound images by using an incremental self-organized map. *23rd Annual International Conference of the IEEE-EMBS*.
- Lippmann, R.P., (1987). An introduction to computing with neural nets. *IEEE ASSP Magazine*, pp. **4-22**.
- Olmo, C.M., Hernandez, F.A., (2000). Computing geostatistical image texture for remotely sensed data classification. *Computer & Geosciences* 26 (4), **373-383**.
- Ölmez, T., Dokur, Z., Yazgan, E., (1996). MR image classification by the neural network and the genetic algorithms. *18th Annual International Conference of the IEEE-EMBS*, paper no.1039.
- Parkkinen, J., Oja, E., (1990). Detecting texture periodicity from co-occurrence matrix. *Pattern Recognition Letters* 11, **43-50**.
- Qian, L.S., Xiang, L., Cheng, L.K., Liang, L.S., (1998). Tissue classification of multi-spectral MR images of brain. *20th Annual International Conference of the IEEE-EMBS*, **634-636**.
- Qian, W., Li, L.H., Clarke, L.P., (1999). Image feature extraction for mass detection in digital mammography-Influence of wavelet analysis. *Medical Physics* 26 (3), **402-408**.
- Reza, N., Ying, S., (1991). Classification of digital angiograms using artificial neural networks. *Annual International Conference of the IEEE-EMBS*, Vol. 13, no. 3, pp. **1440-1441**.
- Serpico, S.B., Bruzzone, L., Roli, F., (1996). An experimental comparison of neural and statistical non-parametric algorithms for supervised classification of remote-sensing images. *Pattern Recognition Letters* 17, **1331-1341**.
- Vinitski, S., Mohamed, F., Gonzalez C. and et al., (1997). Fast tissue segmentation based on a 3D and 4D feature map: Comparison study. *19th Annual International Conference of the IEEE-EMBS*, pp. **505-508**.
- Zhang, W., Yoshida, H., Nishikawa, R.M., Doi, K., (1998). Optimally weighted wavelet transform based on supervised training for detection of microcalcifications in digital mammograms. *Medical Physics* 25 (6), **949-956**.

MONITORING URBAN CHANGES IN ISTANBUL PROVINCE BETWEEN 1992-1995 USING ERS-1 SAR SATELLITE IMAGES

Erhan Alparslan
TUBITAK-MRC Earth and Marine Sciences Research Institute
Anibal Caddesi, Hac Halil Mahallesi, 41470 Gebze-Kocaeli
e-mail:Erhan.Alparslan@posta.mam.gov.tr,
Fax: 0 262 641 23 09, Tel: 0 262 641 23 00 / 4354

ABSTRACT

ERS-1 SAR satellite images of Istanbul Province were each first cleaned by Lee speckle noise filter then transformed into multiple channeled images by texture analysis. Later, these images were visually analyzed and interpreted on the computer screen to determine training areas corresponding to changed urban areas and a neural network was created to establish a back propagating neural network processor.

Key Words: SAR satellite images, Speckle noise removal, Texture analysis, Neural network classifier

ERS-1 SAR UYDU GÖRÜNTÜLERİYLE 1992-1995 ARASINDA İSTANBUL İLİNDEKİ KENTSEL DEĞİŞİKLİKLERİN İZLENMESİ

ÖZET

İstanbul ilinin 1992-1995 ERS-1 SAR görüntülerinin her biri önce Lee süzgeciyle, benek gürültüsünden arındırılmış, doku analiziyle, çok kanallı görüntülere dönüştürülmüştür. Daha sonra bilgisayar ekranında, gözle analiz edilerek ve yorum yapılarak, kentsel değişim alanlarına rastlayan örnek alanlar belirlenmiş, sinir ağı parçası yaratılarak geri yayınlı sinir ağı işlemcisi oluşturulmuştur.

Anahtar Sözcükler: SAR uydu görüntüleri, Benek gürültü süzülmesi, Doku analizi, Sinir ağı sınıflandırıcısı

I- INTRODUCTION

The population of Istanbul Province has been rapidly increasing in an uncontrolled manner due to emigration from various Anatolian provinces. Consequently, some increase in small industry is seen at the expense of increase in housing demands and decrease in forest, park and grassland and green areas, creating a natural phenomenon affecting the ecological status of the entire environment. To study temporal changes in urban areas, SAR satellite images of Istanbul Province acquired in 1992, 1993 and 1995 were employed and Tuzla County was selected as the pilot study area.

Speckle noise inherent in SAR images is a feature, making visual interpretation of such an image a very hard task and originates from not having a one to one signal equality in radar images obtained by active remote sensing methods. The signal transmitted by the active remote sensing platform is scattered by the objects on the earth surface and only some part

of it or itself and its echoes are returned to the receiver on the platform resulting in an unclear image. To remove the speckle noise from the studied images, a filter developed by Lee was first employed then texture analysis was made to produce a multiple channeled input for the neural network classifier.

II- LEE FILTER

The filter proposed by Lee, to remove the speckle noise in images, assumes that the image is both corrupted by additive and multiplicative noises (Lee, 1980, 1981, PCI). Additive and multiplicative noise is defined by the expressions (1-2).

$$z_{i,j} = x_{i,j} + w_{i,j} \quad (1)$$

$$z_{i,j} = x_{i,j} * w_{i,j} \quad (2)$$

In these expressions, $z_{i,j}$ is the received pixel, $w_{i,j}$ is white noise with 0 mean value. The mean value of multiplicative noise is 1. The variance values of

additive and multiplicative noises are unknown because of their local variance. In the model developed by Lee, the value of the pixel in low contrast areas approaches to local mean value, thus noise disturbing the human eye in flat areas, is removed. In high contrast areas, where edges, sharp features and lines exist, the value of the filtered pixel approaches corrupted pixel value, keeping fine details in the image. In local neighborhoods, the variance is above a definite threshold, which may be employed to detect edges in this neighborhood by directional edge detection masks and to remove the noise contaminating the edges. Assuming the presence of both additive and multiplicative noises, a speckle noised SAR image may be filtered by the expression proposed by Lee and given in (3).

$$z_{i,j}^s = \bar{x}_p + \frac{\sigma_p^2 * (x_{i,j} + \bar{x}_p - \sigma_p^2)}{(\sigma_p^2 + \sigma_p^2 + \sigma_+^2)} \quad (3)$$

In this expression, the variables are as defined in (1). σ_p^2 is the additive noise variance assuming the variance value in flat areas is zero. The value 382 calculated in the sea part of the study area was set to additive noise variance. Raw image of the study area, Tuzla County acquired in 1995 by ERS-1 satellite and its by Lee filter cleaned version is depicted in Figure 1.

III- TEXTURE ANALYSIS

In the description of images, pixel color and brightness are commonly used parameters. A less often used parameter is the texture (graininess) (Haralick et al., 1973, 1979, PCI). As opposed to color and brightness (which are associated with 1 pixel) texture is computed from a set of connected pixels (Connors et al., 1980). There are several paradigms for measuring texture mathematically. A commonly used one is based on the so-called gray level co-occurrence matrix (GLCM) (also called gray level dependency matrix in the literature). A GLCM is a two-dimensional histogram

of gray levels for a pair of pixels, which are separated by a fixed spatial relationship. The GLCM approximates the joint probability distribution of a pair of pixels. Most of the texture measures are computed from GLCM directly. In addition, some texture measures are computed from a gray level difference vector (GLDV), which itself is derived from a GLCM. The texture of an image is related to the gray level joint probability distribution, which is approximated by the co-occurrence matrix. If texture measures would not directionally change, GLCM's at (0, 45, 90, 135 degrees) are added up before computing texture parameters. GLDV, sums the absolute differences of the occurrence of the processed pixel to the neighboring pixel. For example, 0 element of GLDV counts the times the difference became 0, i.e. the value of the neighbor pixel is equal to the value of the processed pixel, the element 1, counts the times, when the absolute difference between the processed and the neighboring pixel is 1, i.e. the difference is +1 or -1. GLDV is derived from GLCM by adding the matrix elements in parallel rows to the main diagonal. The texture of an image is related to the gray level joint probability distribution approximated by gray level co-occurrence matrix. Particularly, the amount of dispersion that the GLCM elements have about the diagonal, characterizes the texture of the local region. A small dispersion means that the texture is coarse compared to the length of the spatial relationship.

The different texture measures used in texture analysis are as follows. Here, N is the number of gray levels. P is the normalized symmetric GLCM of dimension N x N. V is the normalized gray level difference vector of dimension N.

$$\sum_{i=0}^{N-1} \sum_{j=0}^{N-1} P(i, j) = 1, \quad (4)$$

$$V(k) = \sum_{i=0, \forall |i-j|=k}^{N-1} P(i, j)$$

These parameters convert a one-channelled image into a multi-channel image, appropriate for inputting into pattern recognition algorithms and classification into interest classes (PCI, Haralick, 1979).

$$\text{Homogeneity, } \sum_{i=0}^{N-1} \frac{P(i,j)}{(1+(i-j)^2)} \quad (5)$$

$$\text{Contrast, } \sum_{i=0}^{N-1} p(i,j) * (i-j)^2$$

$$\text{Dissimilarity, } \sum_{i=0}^{N-1} p(i,j) * |i-j| \quad (6)$$

$$\text{Mean, } \bar{i} = \sum_{j=0}^{N-1} i * P(i,j)$$

$$\text{Variance, } \sigma_1^2 = \sum_{j=0}^{N-1} P(i,j) l * (i-\bar{i})^2$$

$$\text{Standard deviation, } \sigma_1 = \sqrt{\sigma_i^2} \quad (7)$$

$$\text{Entropy, } \sum_{j=0}^{N-1} -P(i,j) \log_e(P(i,j))$$

$$\text{(assuming } 0 * \log_e(0) = 0) \quad (8)$$

$$\text{Angular 2.moment, } \sum_{j=0}^{N-1} -P(i,j)^2 \quad (9)$$

$$\text{Correlation, } \frac{\sum_{j=0}^{N-1} P(i,j) * (i-\bar{i})(j-\bar{j})}{\sqrt{\sigma_i^2 \sigma_j^2}}$$

$$\text{GLDV angular second moment, } \sum_{j=0}^{N-1} V(k)^2 \quad (10)$$

As shown above, some of the textural measures relate to specific textural characteristics of the image, such as the texture element size and the contrast. Others characterize the complexity and nature of gray level transitions, which occur in the image. Even though these features contain information about the textural characteristics of the image, it is hard (if not impossible) to identify which specific textural characteristic is represented by each of these features.

The first nine texture parameters derived from texture analysis of the study area are depicted in Figure 2.

IV- NEURAL NETWORK CLASSIFICATION

A neural network consists of interconnected processing elements call units, nodes or neurons. These are organized in two or more layers (PCI, Bischoff et al., 1992). There is an input layer of units, which are activated by the input image data. The output layer of units represents the output classes to train for. In between, there are usually one or more hidden layers of units (units which are neither input units or output units). A unit in one layer is connected to all units in the next layer. A unit in a hidden or output layer receives input from all units in the previous layer and produces one output value. Each link from a unit to the next layer's units has a weight, which suppresses or allows the output value from the unit. To calculate the output from a hidden layer unit or output layer unit, the net input to that unit is calculated first. Once the net input to the unit is added up, this value is put through an activation function to produce the unit's output: Once the network has been trained, the input image data is used to activate the input layer, going forward through the network and activating the output layer units to produce the output image. Neural network classification of 1992, 1993 and 1995 ERS-1 satellite images of the study area into 6 different urban textures are given in Figure 3.

V- CONCLUSIONS

Changes in urban texture of Istanbul Province were studied in the years 1992,1993 and 1995, selecting Tuzla County as the pilot study area. ERS satellite images of the county were first cleaned by Lee speckle noise removal filter. A comparison of Figure 1b with Figure 1a clearly indicates that Lee filtering is an indispensable operation that must be applied on radar images in order to obtain an image, which is much better for visual interpretation than the unprocessed

radar image displayed on the computer screen. Similar results were also obtained for the images of the year 1992 and 1993, when Lee speckle noise removal filter was applied. This technique works not only for the images studied but also for a broad variety of radar images, smoothing the images while keeping the edge information necessary for their visual interpretation. One of the questions that comes into mind is that speckle noise filtering operation might destroy the texture features, upon which this study is based. However, this is not true, because texture parameter generation from speckle noise cleaned images yield the pure texture parameters free of speckle noise, which would otherwise ruin the accuracy of the classification results.

Texture analysis offers a unique method to map one-dimensional data into multi-dimensions, to facilitate application of pattern recognition techniques. Besides, data in each dimension presents a unique texture parameter, such as homogeneity, mean, standard deviation, contrast, entropy, angular second moment, etc. helping to identify a particular pattern inherent in a particular class.

Tuzla County's 1992, 1993 and 1995 images were displayed in three different image windows on the

computer screen and urban changes were visually interpreted. Changes in urban area along the marina, on the coast, to the south of E5 highway and to the north of E5 highway, the sea and the ships were investigated by taking test areas for each of these visually identified classes. The neural network analysis shows that the neural network classifier is well trained for the test sites and it would not confuse the class of each test site element, by classifying it to the right class. The entire image was then classified into the above-mentioned six classes. The analysis showed that there was some urban growth along the coast, particularly in the man-made structures, like the buildings. Since the number of ships in the marina vary from year to year, some changes were also detected here. Although there was some urban growth in the area to the south of E5 highway, no significant change was visible in the area to the north of E5 highway. Here, there is restricted military area, which accounts for this result. Some areas on the land show similar characteristics to that of the sea, resulting in some minor confusion. However, this might be easily corrected by a further processing of the resulting image, taking into account the sea and the land boundaries, which are evident in the images.

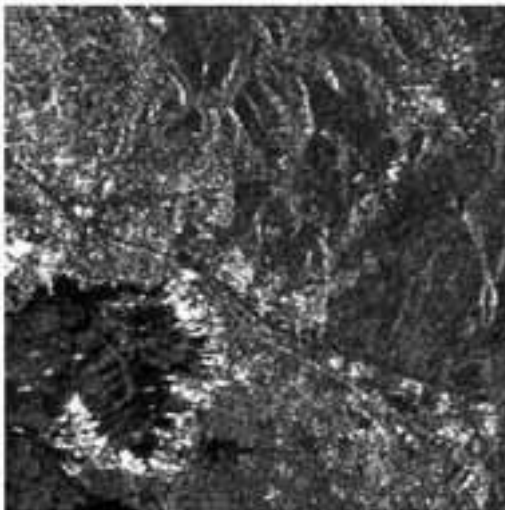


Fig. 1a. Tuzla 1995 ERS-1 satellite image

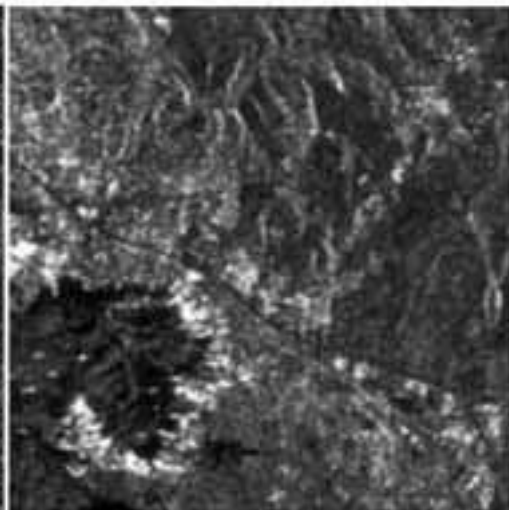


Fig. 1b. Lee filter processed image

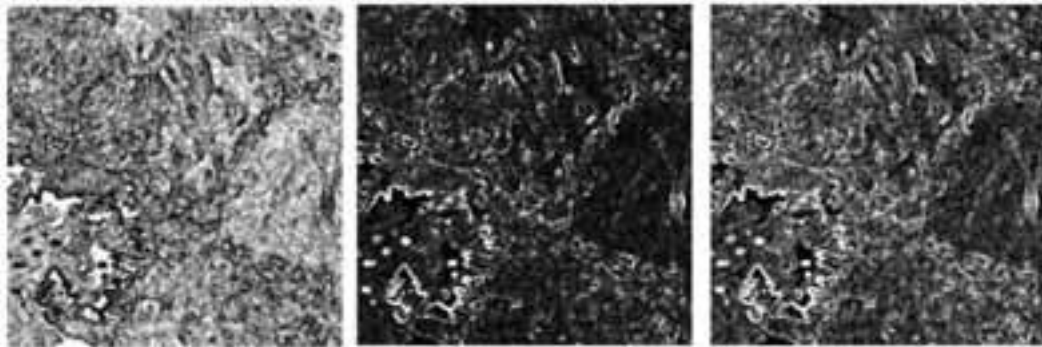


Fig. 2a. Homogeneity

Fig. 2b. Contrast

Fig. 2c. Dissimilarity

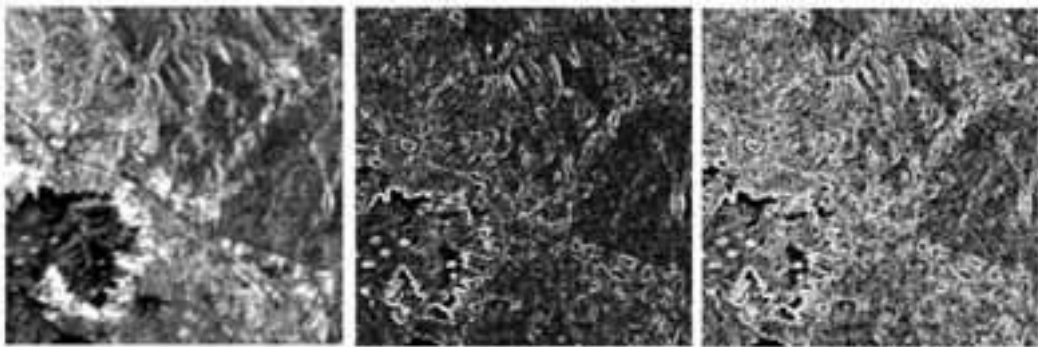


Fig. 2d. Mean

Fig. 2e. Standard Deviation

Fig. 2f. Entropy

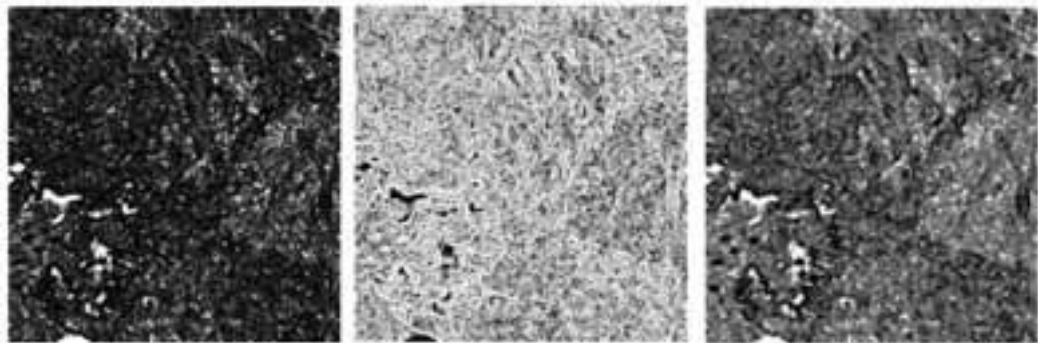


Fig. 2g. Angular 2. Moment

Fig. 2h. Correlation

Fig. 2i. GLDV Ang. 2.M.

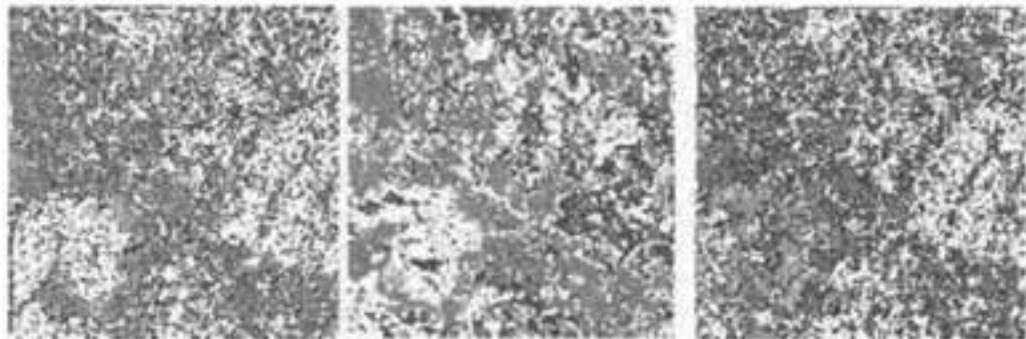


Fig. 3a. (1992)

Neural Network Analyses in Tuzla County

Fig. 3b. (1993)

Fig. 3c. (1995)

REFERENCES

- PCI Image Processing Software Online Manual
Lee, S., (1980). Digital Image Enhancement And Noise Filtering By Local Statistics, *IEEE Trans on Pattern Analysis and Machine Intelligence*, **PAMI-2, 2**, pp.165-168.
- Lee, S., (1981). Speckle Analysis and Smoothing of Synthetic Aperture Radar Images, *Computer Graphics and Image Processing*, **17**, pp. 24-32.
- Lee, J.S. (1981). Refined Filtering of Image Noise Using Local Statistics, *Computer Graphic and Image Processing*, **15**, pp. 380-389.
- Connors, R.W., Harlow, C.A., (1980). A Theoretical Comparison of Texture Algorithms, *IEEE Trans. on Pattern Analysis and Machine Intelligence*, **Vol. TAMI-2, No. 3**, pp. 204-222
- Haralick, R.M., Statistical and Structural Approaches to Texture, *Proceedings of the IEEE*, **67, 5**, pp. 786-804.
- Haralick R.M., Shanmugan K., Dinstein I., (1973). Textural Features for Image Classification, *IEEE Trans on Systems, Man, and Cybernetics*, **SMC-3, 6**, pp. 610-621.
- Bischof, H., Schneider, W., Pinz, A.J., (1992). Multispectral Classification of Landsat-Images Using Neural Networks, *IEEE Trans. on Geoscience and Remote Sensing*, **30, 3**, pp. 482-490

EFFECTS OF THE COLLISIONS ON THE PHASE AND GROUP VELOCITIES OF HF WAVES PROPAGATING IN THE IONOSPHERE AROUND REFLECTION POINTS

Mehmet AYDOĞDU, Esat GÜZEL and Ali YEŞİL
Fırat University, Faculty of Arts and Sci. Department of Physics, Elazığ - TURKEY
Tlf: 0 424 2370000/3260 , Fax: 0 424 2330062 , email : maydogdu@firat.edu.tr
Tlf: 0 424 2370000/6203 , Fax: 0 424 2330062 , email : eguzel@firat.edu.tr
Tlf: 0 424 2370000/6210 , Fax: 0 424 2330062 , email : ayesil@firat.edu.tr

ABSTRACT

In this study, the effects of the collisions on the electromagnetic waves propagating in the ionosphere have been studied. It is shown that the departures from the squares of the real part of the refractive index and phase velocity, group refractive index and group velocity without collisions are proportional to $Z^2(=v^2/\omega^2)$ when the wave frequency $X(=\omega^2/\omega_p^2) < 1$. The departure of the damping factor without collisions is proportional to Z . The maximum effects on these parameters are obtained around reflection points.

Key words: Refractive index, Group refractive index, Phase velocity, Group velocity, HF wave propagating in the ionosphere.

İYONKÜRE PLAZMASI İÇİNDE İLERLEYEN HF DALGALARIN FAZ VE GRUP HIZLARINA YANSIMA NOKTALARINDA ÇARPI MALARIN ETKİSİ

ÖZET

Bu çalışmada, çarpışmaların iyonküre içinde ilerleyen elektromanyetik dalgaların üzerine etkisi çalışılmıştır. Çarpışmaların, $X(=\omega^2/\omega_p^2) < 1$ frekanslarındaki dalgaların kırılma indisinin reel kısmının ve faz hızının karesini, grup kırılma indisi ve grup hızını çarpışmasız haldeki büyüklüklerinden $Z^2(=v^2/\omega^2)$ ile orantılı olarak saptırdığı gösterilmiştir. Sönüm faktörünün çarpışmasız haldeki büyüklüklerinden sapması Z ile orantılıdır. Bu parametrelerin üzerine en fazla etki yansımaya noktası civarındadır.

Anahtar sözcükler: Kırılma indisi, Grup kırılma indisi, Faz hızı, Grup hızı, İyonkürede HF dalga yayılımı.

INTRODUCTION

Electromagnetic waves propagating in the ionosphere are subject to some attenuation because the motions of the electrons and ions are damped through the collisions with other particles. Theoretically, the concept of the group velocity and group refractive index are useful for studying of the propagation of the radio waves in the ionosphere. In earlier studies (Alpert, 1980; Budden and Stott, 1980; Hagfors, 1984; Lundborg and Thide, 1986; Budden, 1988; Zhang, 1991; Aydoğdu and Özcan, 1996; 2001) are made certain assumptions such as the ambient geomagnetic field is vertical and collisionless plasma which are unrealistic in the ionosphere, or it is assumed that Z has no effect on the high frequency waves. However, the conductivity and refractive index of the ionospheric plasma depend on the collisions of the particles. Hence, reflection and refraction conditions change with collisions. In this

paper, the effects of the collisions on the refractive and group refractive indices, phase and group velocities of the wave at reflection points have been studied.

WAVE EQUATIONS

It is assumed that the velocity and the fields vary as $e^{i(k.r-\omega t)}$. Then, Maxwell's equations become

$$\nabla \times E = i\omega B \quad (1)$$

$$\nabla \times B = \mu_0 \sigma E - i\omega \epsilon_0 \mu_0 E \quad (2)$$

From these equations, the following wave equation can be obtained

$$n^2 E - n(n \cdot E) = \left[I + \frac{i}{\epsilon_0 \omega} \sigma \right] \cdot E \quad (3)$$

in which I is unit matrix and (σ) is conductivity tensor of the ionospheric plasma. By using the geometry in Fig. 1, Eq. (3) can be written as

$$\begin{bmatrix} M_{xx} & M_{xy} & M_{xz} \\ M_{yx} & M_{yy} & M_{yz} \\ M_{zx} & M_{zy} & M_{zz} \end{bmatrix} \cdot E = 0 \quad (4)$$

where

$$M_{xx} = n^2 - 1 - \frac{i}{\epsilon_0 \omega} \sigma_{xx},$$

$$M_{xy} = -\frac{i}{\epsilon_0 \omega} \sigma_{xy}, \quad M_{xz} = -\frac{i}{\epsilon_0 \omega} \sigma_{xz}$$

$$M_{yx} = -\frac{i}{\epsilon_0 \omega} \sigma_{yx},$$

$$M_{yy} = n^2 - 1 - \frac{i}{\epsilon_0 \omega} \sigma_{yy}, \quad M_{yz} = -\frac{i}{\epsilon_0 \omega} \sigma_{yz}$$

$$M_{zx} = -\frac{i}{\epsilon_0 \omega} \sigma_{zx},$$

$$M_{zy} = -\frac{i}{\epsilon_0 \omega} \sigma_{zy}, \quad M_{zz} = -1 - \frac{i}{\epsilon_0 \omega} \sigma_{zz}$$

CONDUCTIVITY TENSOR

At high frequency, the effects of ions can be neglected. If V and m are the velocity and mass of electron respectively, the force acting on the electron is

$$m \frac{dV}{dt} = -e[E + V \times B] - m\nu V \quad (6)$$

where $\nu = \nu_{ei} + \nu_{en}$ in which

$$\nu_{ei} = N \left[59 + 4.18 \log \left(\frac{T_e^3}{N} \right) \right] \times 10^{-6} T_e^{-3/2}$$

and $\nu_{en} = 5.4 \times 10^{-16} N_n T_e^{1/2}$ are electron-ion and electron-neutral collision frequencies, respectively (Rishbeth and Garriott, 1969). The standard notation of magnetoionic theory is used. The symbols used stand for

n : refractive index

μ' : real part of group refractive index

N : electron density

N_n : neutral density

T_e : electron temperature

$J (= eNV)$: electron current density

ω_p : angular plasma frequency

ω : angular frequency of wave

ω_c : electron gyrofrequency. These are ,

$$\omega_{cx} = \frac{eB_x}{m}, \quad \omega_{cy} = \frac{eB_y}{m}, \quad \text{and} \quad \omega_{cz} = \frac{eB_z}{m},$$

$$\text{and} \quad Z = \frac{\nu}{\omega}, \quad X = \frac{\omega_p^2}{\omega^2}, \quad Y = \frac{\omega_c}{\omega}$$

$Y_x = Y \cos I \sin d$, $Y_y = Y \cos I \cos d$, $Y_z = -Y \sin I$, where I and d are the magnetic dip and declination angles, respectively. The current density is

$$J = \sigma_0 E - \frac{e}{m(\nu - i\omega)} J \times B \quad (7)$$

where $\sigma_0 \left(= \frac{Ne^2}{m(\nu - i\omega)} \right)$ is the longitudinal conductivity. We assumed that the z-axis of the coordinate system with its origin located on the ground is vertical upwards. The x-axis and y-axis are geographic eastward and northward in the northern hemisphere, respectively. The geometry of the geomagnetic field in the northern hemisphere is given in Fig. 1. Hence,

$$B = B_x a_x + B_y a_y + B_z a_z \quad (8)$$

where $B_x = B \cos I \cos d$, $B_y = B \cos I \sin d$ and $B_z = -B \sin I$. In a cartesian coordinates system, the solution of the Eq. (7) can be written as

$$J = \sigma \cdot E \quad (9)$$

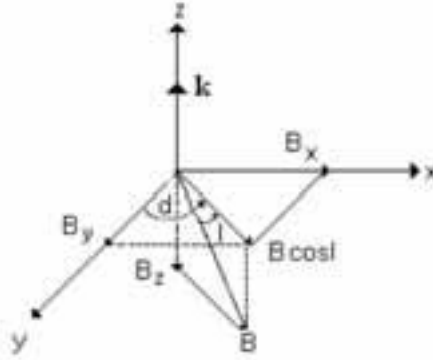


Fig.1. The geometry of Earth's magnetic field and k (Aydoğdu and Özcan, 1996, 2001).

with

$$\sigma = \begin{bmatrix} \sigma_{xx} & \sigma_{xy} & \sigma_{xz} \\ \sigma_{yx} & \sigma_{yy} & \sigma_{yz} \\ \sigma_{zx} & \sigma_{zy} & \sigma_{zz} \end{bmatrix} \quad (10)$$

where

$$\begin{aligned} \sigma_{xx} &= \Gamma \sigma_0 [\omega_{cx}^2 + (\nu - i\omega)^2], \\ \sigma_{xy} &= \Gamma \sigma_0 [\omega_{cx} \omega_{cy} - \omega_{cz} (\nu - i\omega)], \\ \sigma_{xz} &= \Gamma \sigma_0 [\omega_{cx} \omega_{cz} + \omega_{cy} (\nu - i\omega)], \\ \sigma_{yx} &= \Gamma \sigma_0 [\omega_{cx} \omega_{cy} + \omega_{cz} (\nu - i\omega)], \\ \sigma_{yy} &= \Gamma \sigma_0 [\omega_{cy}^2 + (\nu - i\omega)^2], \\ \sigma_{yz} &= \Gamma \sigma_0 [\omega_{cy} \omega_{cz} - \omega_{cx} (\nu - i\omega)], \\ \sigma_{zx} &= \Gamma \sigma_0 [\omega_{cx} \omega_{cz} - \omega_{cy} (\nu - i\omega)], \\ \sigma_{zy} &= \Gamma \sigma_0 [\omega_{cy} \omega_{cz} + \omega_{cx} (\nu - i\omega)], \\ \sigma_{zz} &= \Gamma \sigma_0 [\omega_{cz}^2 + (\nu - i\omega)^2] \text{ with} \\ \Gamma &= [\omega_{cx}^2 + \omega_{cy}^2 + \omega_{cz}^2 + (\nu - i\omega)^2]^{-1} \end{aligned} \quad (11)$$

WAVES AND THEIR REFRACTIVE INDICES

The normal modes of the system are accordingly given by the determinant of Eq.(4)

$$\det(M) = 0 \quad (12)$$

Eq. (12) is the basic dispersion relation. The refractive index n can be obtained in terms of plasma parameters. The electromagnetic wave travelling in the z direction as in the vertical sounding of the ionosphere, the solution of Eq.(12) gives two modes. These are

1) Plasma oscillations

$$\omega_p^2 = \omega^2 + iZ\omega^2 \quad (13)$$

2) Polarization waves (P - waves)

$$n_p^2 = 1 - \frac{X(1 \mp Y_z)}{(1 \mp Y_z)^2 + Z^2} + iZ \frac{X}{(1 \mp Y_z)^2 + Z^2} \quad (14)$$

where, right (-) and left (+) - handed polarization waves. When the wave propagated in the z -direction, there is also a wave which is travelling in the y (or x) direction because of the geometry of the geomagnetic field. These are

1) Ordinary wave (O - wave)

$$n_0^2 = 1 - \frac{X}{1 + Z^2} + iZ \frac{X}{1 + Z^2} \quad (15)$$

2) Extraordinary wave (X - wave)

$$n_x^2 = 1 - \frac{aX(1-X) + Z^2X(2-X)}{a^2 + b^2} + iZ \frac{X(1-X)(2-X) - aX}{a^2 + b^2} \quad (16)$$

where, $a=1-X-Y_z^2-Z^2$ and $b=Z(2-X)$. If electron collisions are allowed for refractive index $n^2 = (\alpha + i\beta)^2 = M + iN$ becomes complex. Real (α) and imaginary (β) are

$$\alpha^2 = \frac{1}{2} \left[(M^2 + N^2)^{1/2} + M \right] \quad (17)$$

$$\beta^2 = \frac{1}{2} \left[(M^2 + N^2)^{1/2} - M \right] \quad (18)$$

The collisions of the electrons with other particles affect on the real and imaginary part of refractive index. The real part of refractive index associate with the phase velocity $V_p (=c/\alpha)$ and the imaginary part of refractive index β with the factor of absorption. Z becomes $Z \ll 1$ at the high frequency (HF) waves. Therefore, the expression of $(1+Z^2)^{-1}$ can be approximated to $(1-Z^2)$ by using binomial expansion. By using this approximation, the real and imaginary parts of refractive index of P-wave (Eq.(14)), O-wave (Eq.(15)) and X-wave (Eq.(16)) and their phase velocities have been obtained. These equations are

O - Wave :

The real and imaginary parts of refractive index of ordinary wave which is given in Eq. (15) and the phase velocity of wave becomes for $X < 1$ as follows,

$$\alpha_0^2 \approx (1-2) + Z^2 \frac{X(4-3X)}{4(1-X)} \text{ and } V_{op}^2 = \frac{c^2}{\alpha_0^2} \quad (19)$$

$$\beta_0^2 \approx Z^2 \frac{X^2}{4(1-X)} \quad (20)$$

P - Wave :

The wave giving in Eq.(14) (right polarization) is depending on geomagnetic field. If Z' and X' are expressed as $Z' = \frac{Z}{1+Y_z}$ and $X' = \frac{X}{1+Y_z}$ polarization wave is becoming the ordinary wave form giving by Eq.(15). For $X' < 1$ the real and imaginary parts of Eq.(14) and phase velocity of the wave are

$$\alpha_p^2 \approx (1-X') + Z'^2 \frac{X'(4-3X')}{4(1-X')} \text{ and } V_{pp}^2 = \frac{c^2}{\alpha_p^2} \quad (21)$$

$$\beta_p^2 \approx Z' \frac{X'^2}{4(1-X')} \quad (22)$$

These expressions are same as expressions of Eq.(19-20). Only, the value of resonance frequency is changed.

X - Wave :

For $X < 1$ the real and imaginary parts of refractive index at Eq.(16) and phase velocity as follows.

$$\alpha_x^2 \approx \frac{(1-X)^2 - Y_y^2}{1-X-Y_y^2} + Z^2 \frac{X^2[(1-X)^2 Y_y^2]^2}{4[(1-X-Y_y^2)^3][(1-X)^2 Y_y^2]}$$

$$\text{and } V_{xp}^2 = \frac{c^2}{\alpha_x^2} \quad (23)$$

$$\beta_x^2 \approx Z^2 \frac{X^2[(1-X)^2 + Y_y^2]^2}{4[(1-X-Y_y^2)^3][(1-X)^2 - Y_y^2]} \quad (24)$$

In the collisional medium, n_x^2 goes to infinity for $X=1-Y_y$ and $X=1+Y_y$ while in the collisionless medium, n_x^2 goes to infinity for $X=1-Y_y^2$. These expressions show that the square of the real part of the refractive index departure from magnitudes without collisions is proportional to Z^2 , and the imaginary part of the refractive index departure from magnitude without collisions is proportional to Z .

GROUP REFRACTIVE INDEX AND GROUP VELOCITY

If V_g is the component of the wave packet's velocity in the direction of wave normal, the group refractive index (μ') is obtained by using the expression,

$$\mu' = \alpha + \omega \frac{d\alpha}{d\omega} \quad (25)$$

Group refractive index and group velocity of waves have been obtained for $X < 1$ and $X' < 1$ as follows,

O - Wave :

$$\mu'_0 = (1 - X)^{-1/2} + Z^2 \frac{X(-6X^2 + 15X - 12)}{8[1 - X]^{5/2}} \quad \text{and} \quad V_{og} = \frac{c}{\mu'_o} \quad (26)$$

P - Waves :

$$\mu'_p \approx \frac{2(1 + Y_z) - X'Y_z}{2[1 - Y_z][1 - X']^{1/2}} + Z'^2 \frac{X'[-24 + 30X' - 12X'^2] - X'Y_z[6X' - 3X'^2]}{16[1 + Y_z][1 - X']^{5/2}} \quad \text{and} \quad V_{xg} = \frac{c}{\mu'_{p'}} \quad (27)$$

X - Waves :

$$\mu'_x \approx \frac{(1 - X)^2 + Y_y^2[Y_y^2 + 3X - 2]}{[(1 - X)^2 - Y_y^2]^{1/2}[1 - X - Y_y^2]^{3/2}} + Z^2 \frac{X^2[(1 - X)^2 + Y_y^2][4X - 1 - 3X^2 - 2Y_y^2]}{[(1 - X)^2 - Y_y^2]^{3/2}[1 - X - Y_y^2]^{5/2}} \quad \text{and} \quad V_{xg} = \frac{c}{\mu'_{x'}} \quad (28)$$

As seen from Eq.(26-28), the effects of the collision on the group refractive index and the group velocity are evident. Magnitudes of the group refractive indices (μ') and the group velocities (V_g) of departure from the magnitudes without collision is proportional with Z^2 when $X < 1$.

NUMERICAL SOLUTIONS AND ANALYSIS

The calculations of the equations (19, 21, 23, 26, 27 and 28) have been done for geographic coordinates of (39°E, 40°N and I=55°, d=3°E) from 125 km to hmF2 height. The used plasma parameters have been obtained by using International Reference Ionosphere (IRI) for June at 1200 LT. To obtain the conditions $X < 1$, the used wave frequency in the calculations is taken as 37.722×10^6 rad / sec. This frequency is equal to the plasma frequency of the ionosphere at hmF2 height. The other parameters are $B = 0.4$ Gauss, $R = 10$, $\omega_{ce} = 7.76 \times 10^6$ rad / sec, $Y = 0.206$, $Y_y = 0.118$ and $Y_z = 0.168$. To see the effect of the collisions, the differences between the values of α^2 , V_p^2 , V_g , and μ' at $Z = 0$ condition (the first terms of the equations (19, 21, 23, 26, 27 and 28) and the values of α^2 , V_p^2 , V_g , and μ' at $Z \neq 0$ conditions have been taken. These are

$$\begin{aligned} \Delta\alpha_0 &= \alpha_0^2(Z \neq 0) - \alpha_0^2(Z = 0) & \Delta\alpha_p &= \alpha_p^2(Z \neq 0) - \alpha_p^2(Z = 0) \\ \Delta\alpha_x &= \alpha_x^2(Z \neq 0) - \alpha_x^2(Z = 0) & \Delta V_{op} &= V_{op}^2(Z \neq 0) - V_{op}^2(Z = 0) \end{aligned}$$

$$\begin{aligned} \Delta V_{pp} &= V_{pp}^2(Z \neq 0) - V_{pp}^2(Z = 0) & \Delta V_{xp} &= V_{xp}^2(Z \neq 0) - V_{xp}^2(Z = 0) \\ \Delta\mu'_o &= \mu'_o(Z \neq 0) - \mu'_o(Z = 0) & \Delta\mu'_p &= \mu'_p(Z \neq 0) - \mu'_p(Z = 0) \\ \Delta\mu'_x &= \mu'_x(Z \neq 0) - \mu'_x(Z = 0) & \Delta V_{og} &= V_{og}^2(Z \neq 0) - V_{og}^2(Z = 0) \\ \Delta V_{pg} &= V_{pg}^2(Z \neq 0) - V_{pg}^2(Z = 0) & \Delta V_{xg} &= V_{xg}^2(Z \neq 0) - V_{xg}^2(Z = 0) \end{aligned}$$

The variations of the phase velocity and the group velocity and $\Delta\alpha_o$, $\Delta\alpha_p$ and $\Delta\alpha_x$ of O, P and X waves are shown in Fig.2-5. The effects of the collisions on the refractive and group refractive indices are evident (Fig. 2-3). The refractive indices are not much affected by the collisions between $X \approx 0.4 - 1$ ($h \approx 170-225$ km) and maximum effects occurs around $X \approx 1$ (reflection heights of waves). As shown in figures, the values of the refractive indices of O and P - waves at ($Z \neq 0$) condition are higher than the values of the refractive indices at $Z = 0$ condition (see Fig. 2a). These show that the phase velocities of O and P waves at $Z \neq 0$ condition is smaller than the phase velocities at $Z = 0$ condition (Fig.4a). It is noted that reflection points of O and P waves are different because of the geomagnetic field. The P - waves reflect at about $h \approx 215$ km height while O-waves reflect at about $h \approx 255$ km height. The variations of the group refractive indices of O and P - waves are given in Fig. 3a. The group refractive index decreases with collisions and group velocity increases as shown in Fig. 5.

The results of X-wave are given in Fig. 2b, 3b, 4b, 5c. X-wave has three reflection points. Extraordinary waves show resonance at $X=1-Y_y$ ($h \approx 223$ km) in the collisional ionosphere while it shows resonance at $X=1-Y_y^2$ ($h \approx 240$ km) in the collisionless ionosphere. The collision has no effect on the group velocities of X waves at $X \approx 0.34$ ($h \approx 155$ km and $\omega_p = 22.21 \times 10^6$ rad/sec) (Fig.3b). After this height, the values of V_g in collisional ionosphere is smaller than the values of V_g in the collisionless ionosphere. It is noted that all calculated parameters in figures

increase around $X \approx 0.3$ ($h \approx 130$ km). This is due to Z which increases at these heights as shown in Fig. 6.

CONCLUSIONS

The collisions of the electrons with the other particles affect the refractive and group refractive indices, the phase and group velocities of HF waves propagating in the ionosphere. The maximum effects of the collisions on these parameters are obtained around the reflection heights.

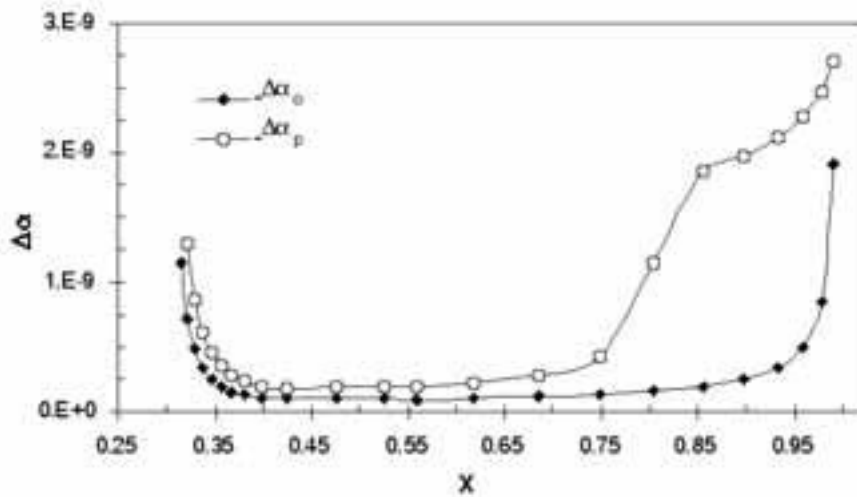


Fig. 2a The variations of $\Delta\alpha_0$ and $\Delta\alpha_p$ with X

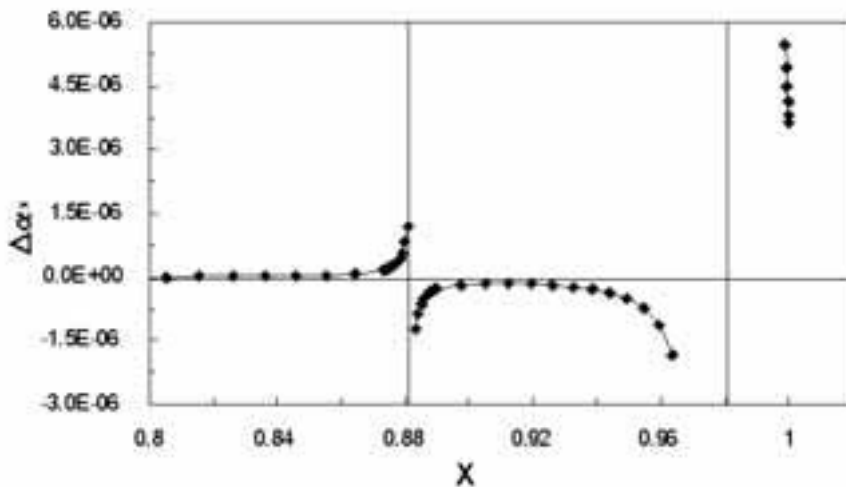


Fig. 2b The variations of $\Delta\alpha_x$ with X

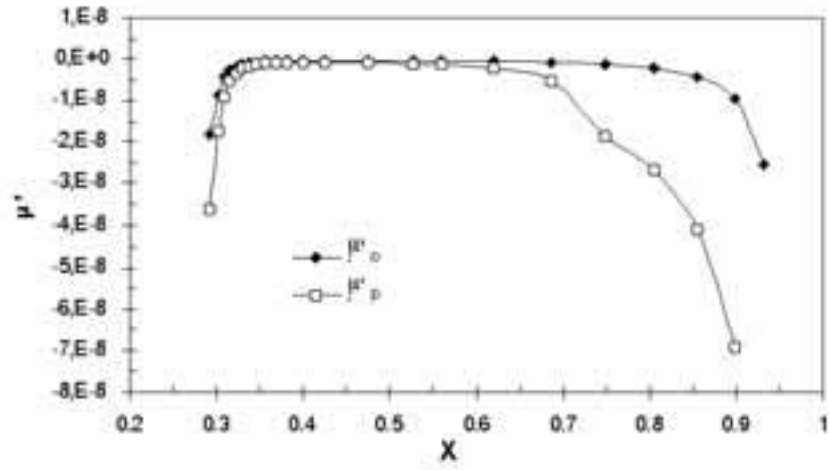


Fig. 3a The variations of $\Delta\mu'_0$ and $\Delta\mu'_p$ with X

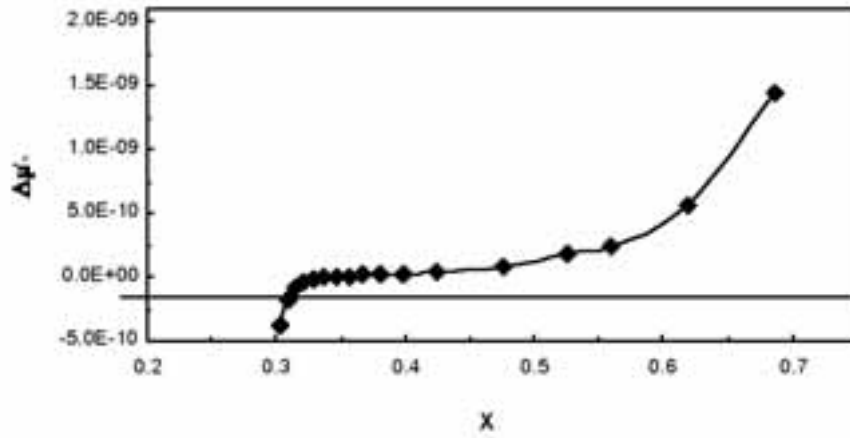


Fig. 3b The variations of $\Delta\mu'_x$ with X

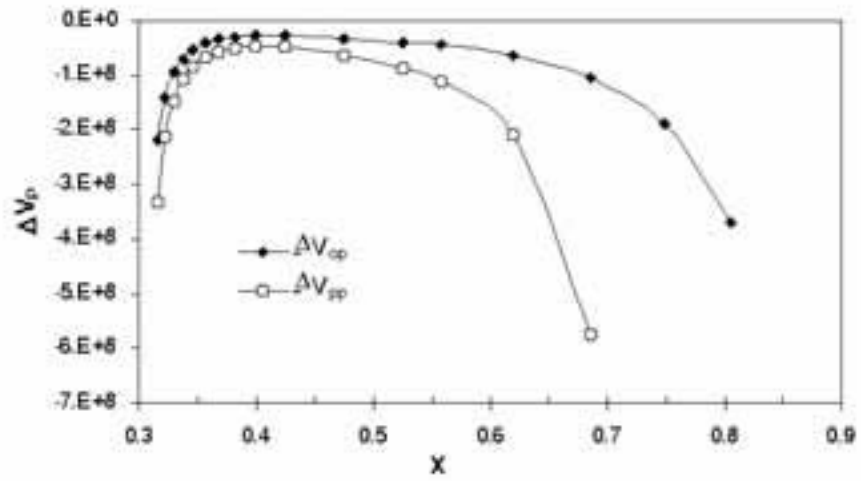


Fig. 4a The variations of ΔV_{op} and ΔV_{pp} with X

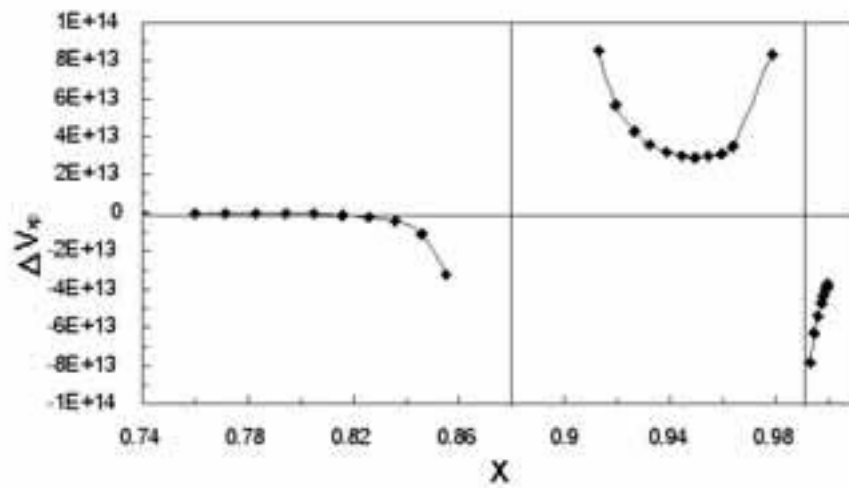


Fig. 4b The variations of ΔV_{sp} with X

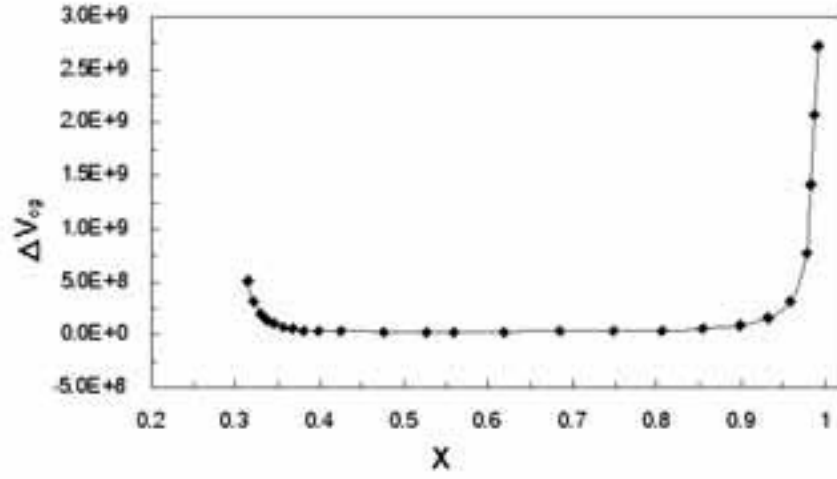


Fig. 5a The variations of ΔV_{og} with X

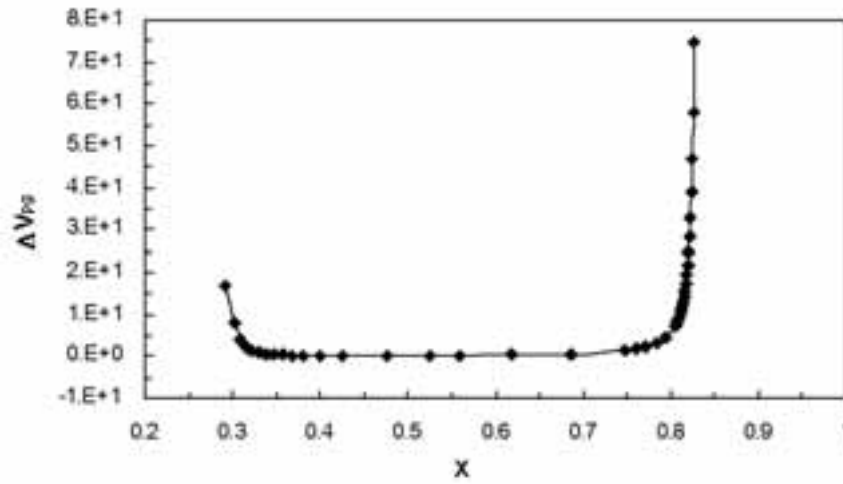


Fig. 5a The variations of ΔV_{pg} with X

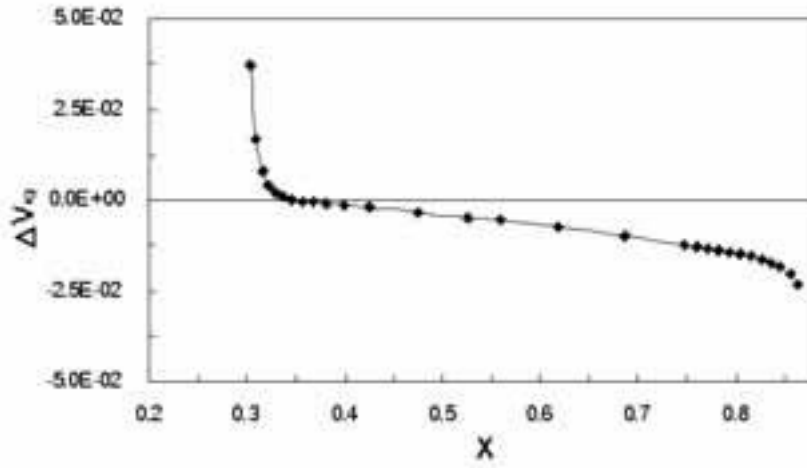


Fig. 5c The variations of ΔV_{xg} with X

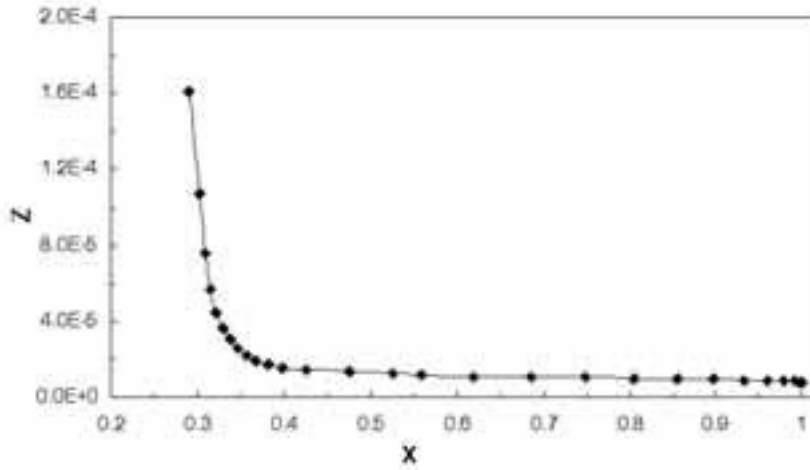


Fig. 6 The variations of Z with X

REFERENCES

- Al'pert, Ya. L., (1980). The direction of the group velocity of electromagnetic waves in a multicomponent magneto-active plasma in the frequency range $0 < \omega < \omega_c$, *J. Atmos. and Solar Terr. Phys.* Vol. 42, **pp. 205-216**.
- Aydođdu, M., O. Özcan, (1996). Effects of magnetic declination on refractive index and wave polarization coefficients of electromagnetic waves in mid-latitude ionosphere, *Indian Journal of Radio and Space Physics*, Vol. 25, **pp. 263-270**.
- Aydođdu, M., O. Özcan, (2000). The possible effects of the magnetic declination on the wave polarization coefficients at the cutoff point, *Progress in Electromagnetic Research, PIER* 30, **pp.179-190**, 2001. Abstract: *J. Electromagnetic Waves and App.*, Vol. 14, **1289-1290**.
- Budden, K.G., G.F. Stott, (1980). Rays in magneto-ionic theory-II, *J Atmos and Solar Terr. Phys.* Vol. 42, **pp. 791-800**.
- Budden, K.G., (1988). *The propagation of Radio Waves*, Cambridge University Press.
- Hagfors, T., (1984). Electromagnetic wave propagation in a field-aligned-striated cold magnetoplasma with application to the ionosphere, *J. Atmos and Solar Terr. Phys.* Vol. 46, **pp. 211-216**.
- Lundborg, B., B. Thide, (1986). Standing wave pattern of HF radio waves in the ionospheric reflection regions 2. Applications, *Radio Science.*, Vol. 21, **pp. 486-500**.
- Rishbeth, H., O. K. Garriott, (1969). *Introduction to Ionospheric Physics*, Academic Press, New York and London.
- Zhang, D.Y., (1991). New method of calculating the transmission and reflection coefficients and fields in a magnetized plasma layer, *Radio Science*, Vol. 26, **pp. 1415-1418**.

REAL TIME COMPUTATION FOR BISTATIC SAR IMAGERY

Mesut Kartal Sedef Kent
Istanbul Technical University, Electrical and Electronics Engineering
Faculty, 80626 Maslak, Istanbul e.mail: mkartal@ehb.itu.edu.tr,
Tel: 0212 28536 29, Fax: 0212 2853565

ABSTRACT

This paper proposes a real time computation method to process of bistatic SAR data. Depending to the application, bistatic SAR measurements are required to enlarge the independent data bank. In the imaging system, the investigation area, which includes the targets moving at any direction is illuminated by a radar antenna, carried on a moving platform. For the monostatic imaging algorithm, each different antenna position measurement on the SAR interval is used to obtain a corresponding image of the observation area. To increase the amount of received data, a second receiver positioned at a different location is used and bistatic synthetic aperture is formed. The additional phase information increases the accuracy of the image. A common solution can be defined to give a finer image by collecting all different observation point results obtained by each antenna. In this paper all processing steps are formulated in time domain. Because of the target and radar platform is in motion, the imaging algorithm requires coherent processing for the phase compensation. Some knowledge about the moving target such as velocity and moving direction of the target is necessary to deal with this compensation.

Key Words: Real Time Imaging, Synthetic Aperture Radar, Bistatic Radar, High Resolution Imaging

BİSTATİK SAR İLE GERÇEK ZAMANDA GÖRÜNTÜLEME

ÖZET

Bu çalışma bistatik SAR verilerinin işlenmesi için gerçek zamanda bir hesaplama yöntemi önermektedir. Uygulamaya bağlı olarak, bağımsız veri bankasını genişletmek için bistatik SAR ölçümlerinin yapılması gereklidir. Görüntüleme sisteminde herhangi bir yönde hareket eden hedefleri içeren incelenen alan hareketli bir platformda bulunan bir radar anteni ile aydınlatılır. Monostatik görüntüleme algoritmasında gözlenen alana karşı gelen görüntüyü elde etmek için SAR açıklığındaki her farklı anten konumu ölçümü kullanılır. Alınan veri miktarını arttırmak için farklı bir konuma yerleştirilen ikinci bir alıcı kullanılır ve bistatik açıklık oluşturulur. Ek faz bilgisi görüntünün doğruluğunu artırır. Her iki antenle farklı gözlem noktalarından elde edilen sonuçların toplanmasıyla daha iyi bir görüntü verecek bir ortak çözüm tanımlanabilir. Bu çalışmada bütün işleme adımları zaman domeninde ifade edilmiştir. Hedef ve radar platformu hareketli olduğundan, görüntüleme algoritması faz düzeltmesi için uyumlu işleme gerektirir. Bu düzeltmeyi yapmak için hareketli hedef hakkında hedefin hızı ve hareket doğrultusu gibi bazı bilgilerin bilinmesi gereklidir.

Anahtar Sözcükler: Gerçek Zamanda Görüntüleme, Sentetik Açıklıklı Radar, Bistatik Radar, Yüksek Çözünürlüklü Görüntüleme

I. INTRODUCTION

Synthetic aperture radar (SAR) applications have been more attractive in recent years on high-resolution target imaging (Mensa, 1991; Wehner, 1995). For a SAR system, the synthetic aperture is formed by moving the radar antenna between any desired positions. A single antenna system is used to receive data in monostatic case, while two-antenna system located on different positions is used for bistatic applications. To obtain more accurate results, it is necessary to get more observations. It is also necessary to obtain the available data containing additional independent information for each measurement.

When the sampling number on the antenna location is kept high, a similar increase will not be observed on the linear independent measurement vectors for all applications. To increase the information rate, bistatic synthetic aperture is formed by using a second receiver antenna at a different location. Therefore the additional phase difference information between the measurement data taken from the two antennas enhances the error minimization and the location information becomes more precise.

One of the important problems in the SAR processing algorithm is error compensation especially relating

the errors caused from motion of the target and measurement system. When the velocity and moving direction of the target are determined, the error correction procedure is applied to the measured data to compensate the phase error. Some methods determining the information about the target motion can be used for this purpose (Delisle and Wu, 1994; Kaiser, 1996; Soumekh, 1995). There are several techniques to improve the radar resolution in azimuth and range direction in SAR systems (Soumekh, 1992; Munson et al. 1983; Moreira, 1994). In many techniques, Fourier domain formulation and FFT computations are used to demonstrate the radar problem and the same techniques are also used to obtain a solution of the inverse problem. The backscattered signals from the target area to the measurement space can be taken into consideration in a processing model such as superposition of the echoed signal. In this work, a discrete formulation is defined in a way to illustrate the problem and an inverse problem can be given by using this formulation. The presented work is related by a SAR imaging system for moving targets. A time domain formulation and its solution are established for imaging algorithm. The proposed processing algorithm does not need any Fourier domain formulation. All computational steps are performed in time domain. This technique gives us some advantages when we observe the results step by step in real time and some simple and fast computation methods such as matrix computation and parallel implementation can be used to reduced the processing time (Kartal et al. 1995).

In the following section, the geometry of the imaging system is given in Fig. 1. The target area is assumed including all moving point targets and the received signal is expressed as a summation of all point target responses. The reflectivity of the targets, trajectory information such as velocity and position are included

in this expression. For bistatic application, the results are compared when the both antennas move on different platforms. The geometry of the bistatic SAR system configuration is shown in Figure 2.

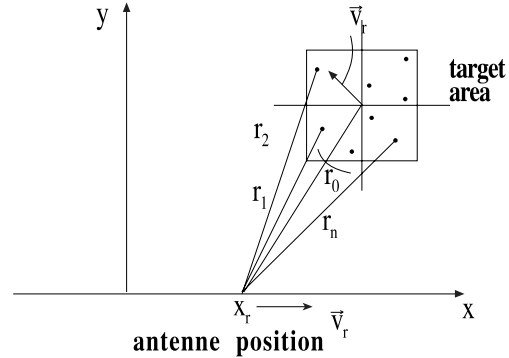


Fig. 1 The geometry of the SAR imaging system.

The inversion algorithm is described in a matrix form. All computations in the inversion algorithm are performed in time domain for both of the antennas in the bistatic geometry. In the following section, the proposed technique for modeling the problem is given. A numerical example is given by applying the algorithm to the synthetic target. The received signal is computed by the algorithm presented in this work.

II. SAR SYSTEM MODEL AND IMAGING ALGORITHM

A two-dimensional SAR imaging geometry is given in Fig. 1. In this system, it is assumed that the radar antenna is located in x-y coordinate system and it moves along the x-axis ($y=0$) with velocity \vec{v}_r . In the same plane, point targets are assumed moving with velocity \vec{v} and a square target area includes all targets. The radar antennas, at any x_{ir} location, illuminate the target area with a pulse $g(t)$ of duration T. Echoed signal is also received at the same x_{ir} position. The round-trip phase delay of the echoed signal is $2R_i/c$, where c is the speed of electromagnetic wave. R_i is

the range of the target is expressed as

$$R_i = \sqrt{(x - x_{ir})^2 + y^2} \quad (1)$$

where index i denotes the antenna number, (i=1,2). When the receiving antenna is at x_{ir} position, the total measured echo signal in observation time t can be expressed as (Kent and Paker, 1996),

$$S_i(x_{ir}, t) = \int_s b(x, y, t) g(t - \frac{2R_i}{c}) dx dy \quad (2)$$

where $b(x,y,t)$ is the target reflectivity function at any x, y position, R_i is the range from this target position to the ith antenna, g is the reference waveform that has delayed roundtrip phase and S is the target investigation area.

In this paper, it is assumed that the target area includes the point targets at any x-y discrete position and the intensities of this discrete point targets are constant when the observation time t is changed. Under these constraints, at any arbitrary time t_j and antenna position x_{ir} the total received signal, which contains a number of N distributed points, is

$$S_i(x_{ir}, t_j) = \sum_{n=1}^N b_n \cdot g(t_j - \frac{2R_{in}}{c}) \quad (3)$$

$j = 1, 2, \dots, M$

where b_n and R_{in} are the intensity and range of the nth target point, respectively, M is the number of measurement during the observation time interval T_m .

If Eq. (3) is rewritten for all discrete observation time t_j ($j=1,2,\dots,M$), the resultant equations can be expressed in a matrix form:

$$[S_j] = [G] [b] \quad (4)$$

In Eq. (4) $[S_j]$ and $[b]$ are the column vectors whose

elements are the echo signals of any t_j instant, and intensities of the point targets, respectively. $[G]$ is a $M \times N$ matrix each of whose row element expresses the round-trip phase delay of the reference signal at an antenna position and time t_j in measurement interval.

To find out the elements of matrix $[G]$, the initial range and velocity of the target area are supposed to be known. There are some methods to obtain these parameters (Delisle and Wu, 1994; Kaiser, 1996; Soumekh, 1995). For example, if we use two receiving antennas, while one of them transmits the signal and both of them are used to receive echo signals from target area, the phase of the receiving signals will be different from one antenna to the other one. The phase difference of two signals can be expressed in terms of two different ranges. This range difference has the information about the target position and the initial angular position. The velocity of the target can be extracted from this information by using an optimization procedure. As an another advantage of the proposed bistatic SAR system, bistatic SAR antennas can also be used to obtain the initial estimates of the target positions and its velocity.

When the target trajectory is estimated, we can express the phase error of the received signal causing from the motion of the target and antenna platform. Then we apply the error compensation to the received signal. After this compensation, it is easy to construct the matrix $[G]$.

It is obvious that the unknown vector $[b_j]$ is found simply by matrix inversion.

$$[b_j] = [G]^{-1} [S_j] \quad (5)$$

Generally the matrix $[G]$ is not a square matrix, but a lot of matrix inversion techniques can be used to find out the inverse matrix (Kartal et al. 1995; Haykin, 1996).

It must be noted that a single antenna measurement

position will not be sufficient, since there is no unique solution. The narrower the solution space, the more antenna observation positions are required. Because of our proposed bistatic SAR system has two transmit/receive antennas, we can collect sufficient data to narrow the solution space. Then, for any different x_{ir} position, a solution of $[b_i]$ can be found from Eq. (4). It is possible to express a common solution by using the vectors $[b_i]$. This process converges the result to a better solution. To increase the accuracy of the algorithm, the number of the discrete measurement instances in T_m duration and the discrete x_{ir} position should be chosen appropriately.

III. NUMERICAL EXAMPLES AND RESULTS

Let us consider the SAR geometry mentioned in Fig. 2. The object is illuminated in (X_1, Y_1+u) and (X_2, Y_2+u) for the synthetic aperture synthesized on the (x, y) plane, and in the aperture $u[-L, +L]$. Receiver antennas record the signal reflected from the object at the coordinates (X_1, Y_1+u) and (X_2, Y_2+u) . Here, (X_1, Y_1) and (X_2, Y_2) are the known constants. A sinc pulse was chosen as the transmitting signal. The resolution of the target area is defined by dividing the area to squared cells. The distance between the receiver point and the center of the target area, and the farrest point to this center are r_0 and a , respectively. Therefore, the observation time interval is limited by,

$$\frac{2(r_0 a)}{c} < t' < \frac{2(r_0 + a)}{c} + T \tag{6}$$

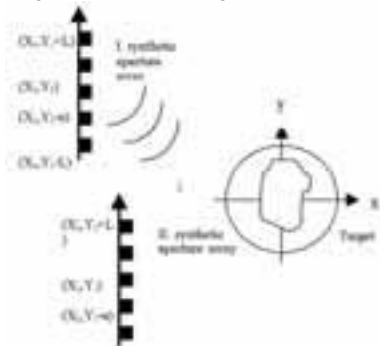


Fig. 2 The geometry of the bistatic SAR imaging system

Numerical simulation parameters of the target and SAR system are given in Table I. The point target distribution selected for the simulation is given in Fig. 3. Obtained results for the monostatic and bistatic antenna cases are shown in Fig. 4 and 5, respectively. In the bistatic case where the second antenna moves in accordance and independent of the first antenna, better results are obtained. Results show that, the location accuracy at the reconstructed image for the bistatic case is better than the monostatic case.

In this work, it must be pointed out that the expressions in our algorithm are used in time domain and the results are obtained in real time. This is important because the results can be observed step-by step. Since the algorithm requires only a matrix inversion, it is effective to reach the results rapidly. Table. I buraya girecek

Table 1. Numerical Simulation Parameters

Target		
Velocity		$\vec{v} = -150\hat{e}_x + 200\hat{e}_y$
x_0		8660 m
y_0		5000 m
Target area dimension		10 m X 10 m
Radar		
Pulse shape		Sinc
Pulse duration		40 nsec
Modulation frequency		3 GHz
Number of measurement in time (N)		20
Number of antenna position (M)		20
$x_r(t=0 \text{ sec})$		-5000 m
$x_r(t=20 \text{ sec})$		5000 m

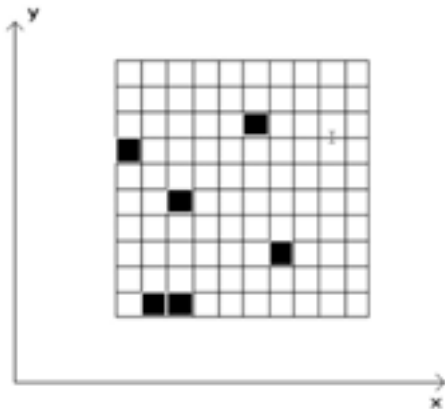


Fig. 3 Point distribution of the selected target.

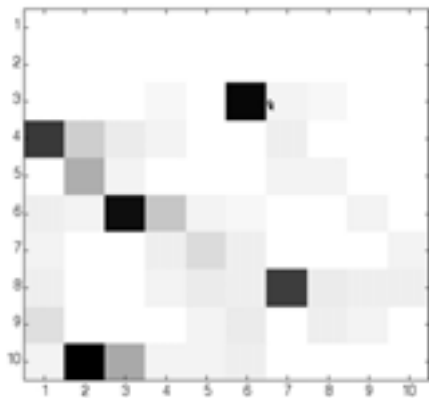


Fig. 4 Obtained SAR image for the stationary receiving antenna.

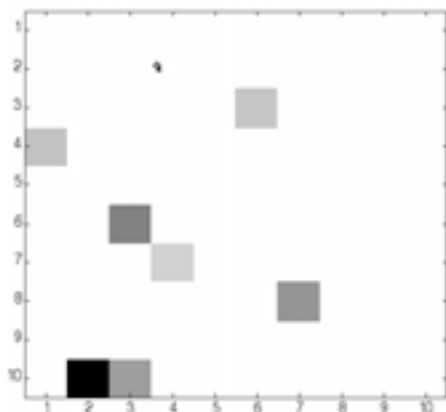


Fig. 5 Obtained SAR image for the second antenna in motion.

IV. CONCLUSIONS

Bistatic real time SAR imaging algorithm described in this paper has some advantages in the processing of information of SAR problem. One advantage of the algorithm is that all computation process is in time domain. The image of the target area can be obtained separately at any antenna measurement position and the results can be observed step by step in the process. Once the matrix G in the algorithm is construct, the inversion algorithm requires only a matrix inversion process for each antenna position. In bistatic SAR application the received data which is obtained by two different antennas gives us more information as compared to the monostatic case and this information has an advantage of finding more accurate results. A high-speed computation technique such as parallel processing can be used to compute the inverses of the matrices separately at the same time. This method reduces the computer time. Since the pulse waveform affects the structure and property of matrix $[G]$, (for example, ill-conditioning), the choice of pulse form and duration are important regarding the accuracy of the solution. The image quality can be enhanced by using an optimization algorithm to give a common solution from the result, which is obtained by each antenna.

REFERENCES

- Delisle G. Y., H. Wu H., (1994). Moving Target Imaging and Trajectory Computation Using ISAR, *IEEE Trans. Aerospace and Elec. Sys.*, **30**, **3**, pp. **884-899**.
- Haykin S., (1996). Adaptive Filter Theory, *Englewood Cliffs*, NJ, Prentice-Hall.
- Kaiser G., (1996). Physical Wavelets and Radar, *IEEE A.P. Magazine*, **38**, **1**, pp. **15-24**.
- Kartal M., B. Yazgan, O.K. Ersoy, (1995). Multistage Parallel Algorithm for Diffraction Tomography, *Applied Optics*, **34**, **8**, pp. **1426-1431**.
- Kent S., S. Paker, (1996). Rejection of Motion Irregularities in SAR Images, *European Conference on Synthetic Aperture Radar*, pp: **147-150**, Koenigswinter, Germany.
- Mensa, D.L., (1991). High resolution radar cross-section imaging, Artech House, MA.
- Moreira A., (1994). Airborne SAR Processing of Highly Squinted Data Using a Chirp Scaling Approach with Integrated Motion Compensation, *IEEE Trans. Geo. and Rem. Sens.*, **32**, **5**, pp. **1029-1040**.
- Munson D.C., J.D. O'Brien, W.K. Jenkins, (1983). A Tomographic Formulation of Spotlight Mode Synthetic Aperture Radar, *Proc. IEEE*, **71**, **8**, pp. **917-926**.
- Soumekh M., (1992). A System Model and Inversion for Synthetic Aperture Radar Imaging, *IEEE Trans. Image Processing*, **1**, **1**, pp. **64-76**.
- Soumekh M., (1995). Reconnaissance with Ultra Wideband UHF Synthetic Aperture Radar, *IEEE Signal Processing Magazine*, **12**, **4**, pp. **21-40**.
- Wehner, D.R., (1995). High Resolution Radar, Norwood, Artech House, MA.

NOVEL T/R ANTENNA DESIGNS FOR SURFACE WAVE HF RADAR SYSTEMS WITH NARROW ELEVATION AND AZIMUTHAL BEAMWIDTHS*

Ahmet Serdar Türk, Burak Polat
TÜB-TAK Marmara Research Center, Information Technologies Research Institute,
P.O.Box 21, 41470, Gebze, Kocaeli
Tel: 0(262) 641 23 00 ext. 4755/4822 Fax: 0 (262) 646 31 87
E-mail: ahmet@btae.mam.gov.tr , polat@btae.mam.gov.tr

ABSTRACT

Over-the-horizon radar and communication systems use T/R antenna systems that depend on surface and sky wave propagation. Surface wave HF radar systems are widely used for detection and identification of targets in ranges up to several hundred kilometers. The T/R antenna systems of the radar are designed depending on the desired look angle, coverage area and scan resolution. In this study some novel T/R antenna configurations with narrow elevation and azimuthal beamwidths are presented for HF radars operating in the surface wave mode and the improvement of the performance and efficiency of the radar antenna system are investigated using Numerical Electromagnetics Code.

Keywords: HF radar, Surface wave propagation, Electronic beam scanning

YÜZEY DALGALI HF RADAR SİSTEMLERİ İÇİN DAR DÜŞEY VE YATAY HUZMELİ VERİCİ/ALICI ANTEN TASARIMLARI

ÖZET

Ufuk ötesi iletişim ve radar sistemlerinde HF bandında yer ve gök dalgası yayılımına dayalı anten sistemleri kullanılmaktadır. Yer (veya yüzey) dalgali HF radarları ufuk ötesinde birkaç yüz kilometrelik menzillerde hedef algılamasına yönelik çalışırlar. Bu radarların verici ve alıcı anten sistemleri, bakış açısı, kapsama alanı ve tarama çözünürlüğüne göre tasarlanmaktadır. Bu çalışmada, radar sistem başarımını ve verimini artırıcı dar huzmeli dizi anten yapıları tasarlanmış, sonuçları değerlendirilerek elde edilen katkılar sunulmuştur.

Anahtar Kelimeler: HF radar, Yüzey dalga yayılımı, Elektronik huzme tarama

I. INTRODUCTION

Over-the-horizon radar and communication systems use T/R antenna systems that depend on surface and sky wave propagation. Surface wave HF radars are capable of detecting and identifying targets for ranges up to several hundred kilometers. Improvement of the power efficiency of the radar system which is designed depending on the desired look angle, coverage area and scan resolution, will have a major influence on the target detection performance. Therefore, the design of the antenna systems with high gain, narrow beamwidth and low back-to-front ratio and take-off angle gains importance in radar systems.

In this study novel antenna array configurations with narrow elevation/azimuthal beamwidth and low side/back lobe level are designed. Therefore the target detection performance for ranges up to several hundred

kilometers can be performed reducing the back scattered ionospheric clutter and increasing the maximum range of the radar. In this context compact antennas comprising elevated linear arrays of short dipoles are designed. Monopole antenna arrays with narrow beamwidth and low side lobe level are synthesized in order to scan electronically a wide aperture on the horizontal plane with high angular resolution. High gain HF antenna structures with narrow beamwidths on both elevation and azimuth planes are realized by integrating horizontal and vertical array structures.

II. ELECTRONIC BEAM SCANNING AT THE RECEIVER ANTENNA SYSTEM

Electronic beam scanning techniques (cf. Ma, 1974) are used in the HF receiver antenna systems aligned in parallel to the shore line, since a mechanical scan,

*This study is sponsored by Turkish Navy Research Center Command (ARMERKOM)

especially for wide coverage areas with narrow beams is impossible for land based systems. Equiphased monopole antennas aligned with a certain separation can provide beamwidths with a few degrees and radiation patterns with 20-30 dB side lobe levels (see Fig. 2). The main beam can be rotated over the horizontal plane when the phase feeds are adjusted to proper values. This process can be implemented by applying a phase delay at the antenna inputs as well as a digital delay at the signal processing block. One of the main difficulties in beam scan is the change of the radiation pattern during scanning and the rise of the side lobe levels to undesired levels

II.1 Array Design Technique

Consider the linear antenna array given in Fig. 1. Let us assume that this structure comprises N antennas each with individual radiation patterns $f_i(\theta, \varphi)$, $i=1,2,\dots,N$ and separation d . The electrical far field of the i -th element with phasor current I_i at a radial distance r_i is given by

$$\vec{E}_i(\theta, \varphi) = \hat{\theta} f_i(\theta, \varphi) I_i \frac{e^{jkr_i}}{r_i}, \quad i = 1, 2, \dots, N. \tag{1}$$

Here, k is the free space wave number.

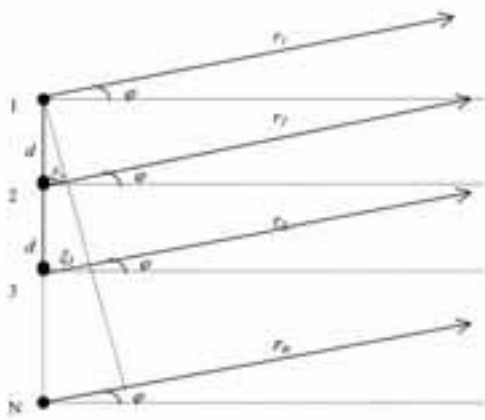


Fig. 1 Linear array beam scanning configuration

When the array elements are chosen identical ($f_i(\theta, \varphi) \equiv f(\theta, \varphi)$), the antenna pattern can be expressed under the far field approximation ($d_N = (N-1)d \ll r_i \forall_i$) as follows:

$$\vec{E}(\theta, \varphi) = \sum_{i=1}^N \vec{E}_i(\theta, \varphi) \tag{2}$$

Substituting (1) into (2) yields

$$\vec{E}(\theta, \varphi) = \hat{\theta} f(\theta, \varphi) \sum_{i=1}^N I_i \frac{e^{jkr_i}}{r_i} \tag{3}$$

One replaces r_i in (3) with

$$r_i = r_1 + \xi_i, \quad i=2,\dots,N \text{ (for phase terms)} \quad r_i \approx r_1, \quad i=2,\dots,N \text{ (for amplitude terms)}$$

under the far field approximation, where $\xi_i = d_i \sin \varphi$. Assuming that the array elements are fed with a phase difference Ψ_i with respect to the first one, the total radiation pattern of the array can be expressed as ($r_i \approx r_1$):

$$\vec{E}(\theta, \varphi) = \hat{\theta} F(\theta, \varphi) \frac{e^{jkr}}{r} \tag{4}$$

$$F(\theta, \varphi) = f(\theta, \varphi) \sum_{i=1}^N I_i e^{j(i-1)(kd \sin \varphi + \Psi_i)}$$

As seen from (4) the total radiation field is proportional to the radiation pattern of a single element and a summation of the currents and phases of the array elements. Despite a number of simplifying assumptions, the array factor still possess a pretty complicated parametric dependence. In beam scanning the main purpose is to determine the optimum phase feeds to direct the main beam at a certain look angle. There may appear differences in patterns on the rotated diagrams with high side and/or back lobe levels. Such minor deficiencies are rather removed by adjusting the current amplitudes. In section 2.2 we shall present a number of numerical design examples to clarify the above statements and comment on removing the deficiencies that arise

II. 2 Numerical Examples

In Figure 2 NEC simulation is depicted for electronic beam scanning of a 16 element quarter wave monopole array placed over dry ground. By adjusting the phase differences in the array elements beam scanning is performed between 0° - 45° with 15° steps. Besides, radiation fields in the presence of sea and dry ground are also analyzed to observe possible changes on the radiation patterns (disregarding the

variation of gain).

During scanning the pattern of antenna gain and radiation field should be preserved while reducing the side lobe levels to a minimum. As seen in Figure 3, the radiation pattern may disorient at large scan angles. Current adjustment is suitable at these cases. Besides, increasing the number of elements will greatly reduce the side lobe levels while their number will increase due to interference.

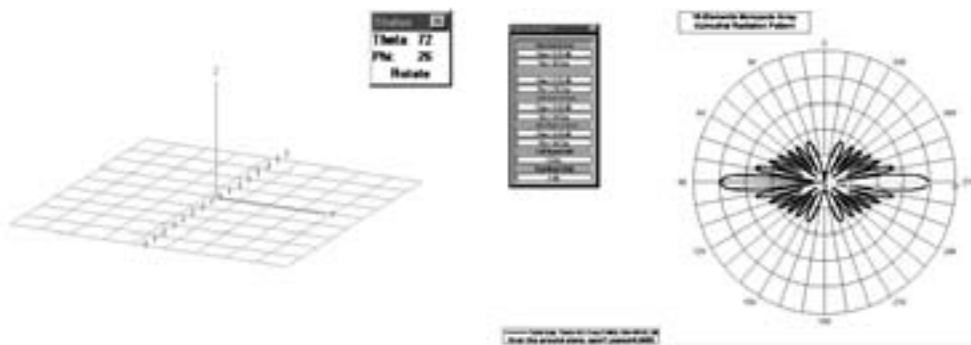


Fig. 2 16-element monopole array and the azimuthal radiation pattern over dry ground (with $\epsilon_r=7$, $\sigma = 3.10^4 S/m$)

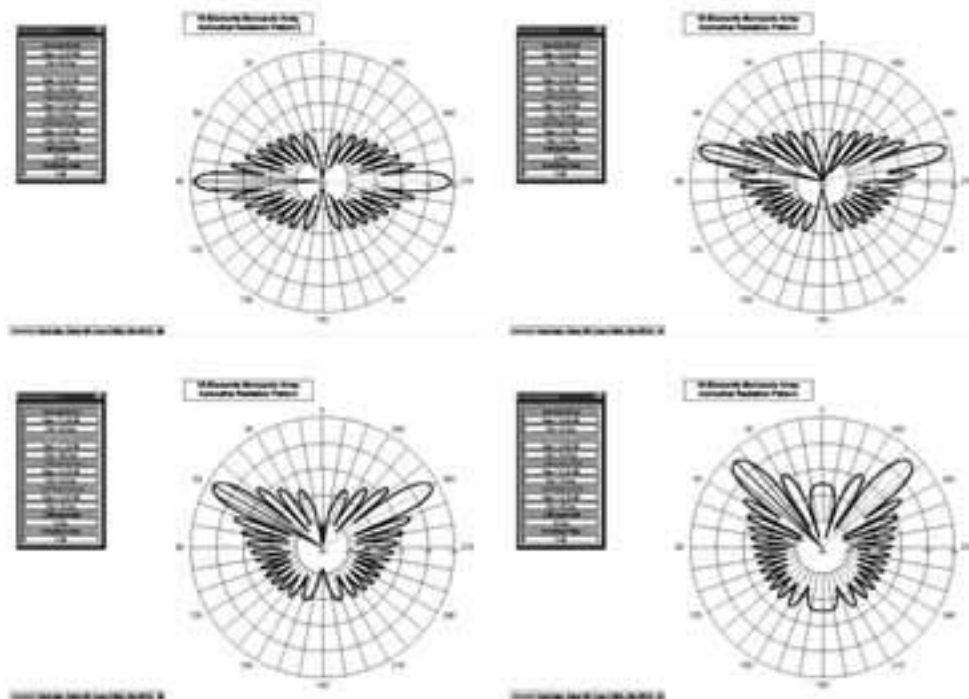


Fig. 3 Antenna diagrams with the beam rotated with 15° steps in the interval 0°-45° over perfectly conducting ground

III. NARROWING THE ELEVATION BEAM FOR T/R ANTENNA ARRAYS

Ionospheric reflection is the typical means of transmission in the HF band to attain great ranges around the earth and the basic principle for sky wave HF radars. Nevertheless, the presence of ionosphere poses a disadvantage for monostatic surface wave HF radar system because of the clutter received at the receiver antenna due to the small part of the power transmitted upwards in the atmosphere (Fien and Polat, 2002). Similarly, the reception of the ionospheric clutter as well as atmospheric noise at

the receiving antenna reduces the system performance seriously. Beside advanced signal processing algorithms, the main solution to remove such deficiencies is obviously to narrow the elevation patterns of T/R antennas and reduce the take-off angle. For this purpose a number of elevated antenna configurations are investigated. Radiation patterns with narrow beamwidth, low back-to-front ratios and small side lobes in the upward direction are presented in Figures 4 and 5 realized with proper phase feeds.

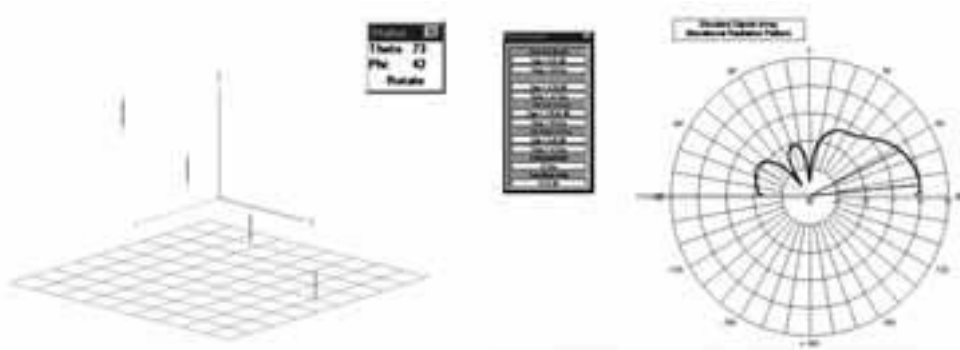


Fig. 4 Elevated transmitter dipole antenna array and vertical radiation pattern over sea surface (with $\epsilon_r=70$, $\sigma = 5 S/m$)

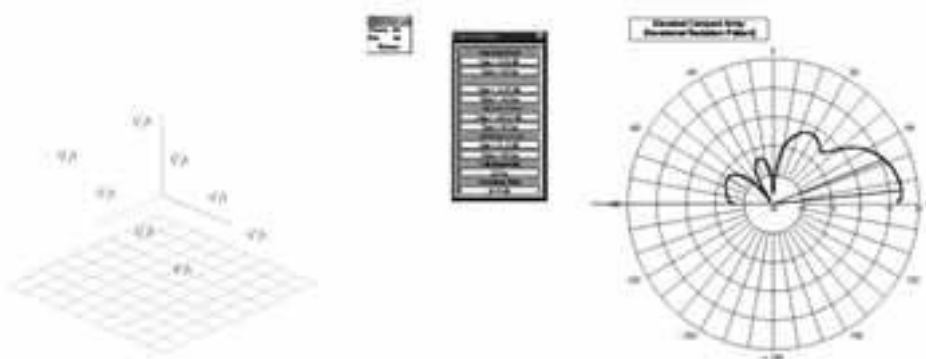


Fig. 5 Elevated compact (pentagon) receiver antenna array and vertical radiation pattern over sea surface (with $\epsilon_r=70$, $\sigma = 5 S/m$)

IV. RESULTS AND CONCLUDING REMARKS

The advantages of using elevated platforms compared to the classical ground based monopole arrays in surface wave HF radar systems are presented. Main advantages can be summarized as greater ranges with improved power efficiency, lower ionospheric clutter and atmospheric noise and less ohmic loss (cf. fien and Türk, 2002) over the antenna ground. Another result is that the vertical radiation pattern and electronic beam scanning are not effected from different grounds such as perfectly conducting, dry

earth, or sea.

The scan efficiency in beam scanning reduces due to the the disorientation of the antenna pattern at large scan angles with the rise of side and back lobes. Therefore circular/elliptical configurations would yield better results for wide angle scanning on the horizontal plane. (cf. (Tanner,1979) for circular arrays). As a next stage of the research the authors plan to employ linear antenna shaped beam synthesis methods to achieve desired elevation and azimuthal patterns for various configurations including the ones presented and referred to in this paper.

REFERENCES

Ma, M.T., (1974). Theory and Application of Antenna Arrays, New York, John Wiley and Sons Inc.

fien, B., B. Polat, (2002). Ionospheric Clutter and its effect on the Performance of Surface Wave HF Radar System Performance, *Proceedings book of URSI-TURKIYE'2002*, pp. 399-402, Istanbul, Turkey.

Tanner, R.L., (1979). A new computer-controlled high frequency direction-finding and transmitter locating system, *Agard Conference Proceedings*, no.263, pp. 45/1-13 Lisbon, Portugal.

fien, B., (2002). A.S. Türk, Ground screen designs for enhancement of surface coupling efficiency for surface wave HF radar systems, to appear in the proceedings book of ELECO' 2002, pp. 140-144, Bursa, Turkey.

ADAPTIVE VOLTERRA FILTERING USING COMPLETE LATTICE ORTHOGONALIZATION

Ender Mete Ek iođlu and Ahmet Hamdi Kayran
Department of Electrical Engineering, Istanbul Technical University, 80626 Maslak, Istanbul, Turkey
Corresponding Author: kayran@ehb.itu.edu.tr (A. H. Kayran), Fax: 0 212 285 3609, Tel: 0 212 285 3563

ABSTRACT

This paper presents a novel method for realizing nonlinear Volterra filters. The novel structure employs the recently developed reduced-order 2D orthogonal lattice filter. An adaptive-second order Volterra filter based on this structure and a recursive least squares adaptation algorithm are presented. In order to confirm the performance of novel structure, simulations for the proposed method and previously published competing realizations are included. The convergence performance of our structure in the adaptive system identification setting is superior to previous models proposed in the literature.

Key Words: Nonlinear systems, Volterra filters, Lattice filters.

KAFES SÜZGEÇ DİKLEŞTİRME KULLANILARAK UYARLAMALI VOLTERRA SÜZGEÇİ GERÇEKLEŞTİRİLMESİ

ÖZET

Bu makalede doğrusal olmayan Volterra süzgeçlerinin gerçekleştirilmesi için 2-Boyutlu (2-B) dik kafes süzgeci kullanan yeni bir yapı önerilmektedir. Özyineli en küçük kareler (RLS) uyarlamalı ikinci dereceden bir Volterra süzgeci gerçekleştirilmektedir. Önerilen yapının ba arımı daha önce yayınlanmış yapılarla karşılaştırılmakta ve etkinliği gösterilmektedir. Sunduğumuz yapının uyarlamalı doğrusal olmayan sistem tanılama uygulamasında ba arımının, daha önce literatürde sunulan yöntemlere göre daha yüksek olduğu bilgisayar benzetimleriyle gösterilmektedir.

Anahtar Sözcükler: Doğrusal olmayan sistemler, Volterra süzgeci, Kafes süzgeç

I. INTRODUCTION

There are a large number of applications where the linear system paradigm fails and one has to resort to nonlinear systems. The truncated Volterra series expansion provides a commonly used nonlinear model (Mathews, 1991). However, polynomial regression models such as the truncated Volterra expansion suffer from ill-conditioning, especially if the degree of the polynomial is high. It is known that even when the input signal is white, the presence of the nonlinear terms in the input vector will cause the eigenvalue spread to be more than one. It is important to seek for alternate Volterra filter realizations that have better numerical properties. Lattice models provide a viable orthogonalized structure (Mathews, 1991; Syed and Mathews, 1994). In Kayran (1996a), an order recursive solution for the 2D normal equations was developed. This has lead to an efficient orthogonal lattice predictor for 2D filtering. This structure has been previously utilized to develop methods for 2D

FIR Wiener filtering (Kayran and Ekfiöđlu, 2000a), 2D ARMA modeling (Kayran, 1996b) and 2D maximum likelihood spectrum estimation (Kayran, 1996c). In this letter, we apply the fully orthogonal 2D lattice structure in (Kayran, 1996a) to the realization and identification of truncated Volterra series expansion based nonlinear systems. This model can be applied to Volterra systems with arbitrary input signals and arbitrary supports for the Volterra kernels, as opposed to some proposed models which are orthogonalizing only for special, e.g. Gaussian input signals and special shapes for the Volterra kernel support (Syed and Mathews, 1994).

II. MATERIALS AND METHODS

II.1 2D Lattice Analysis Model

Consider the nonlinear system with the input-output relation based on the truncated second-order Volterra series expansion.

$$d(n) = \sum_{m_1=0}^{N-1} a_{m_1}(n)x(n-m_1) + \sum_{m_1=0}^{N-1} \sum_{m_2=m_1}^{N-1} b_{m_1,m_2}(n)x(n-m_1)x(n-m_2) \quad (1)$$

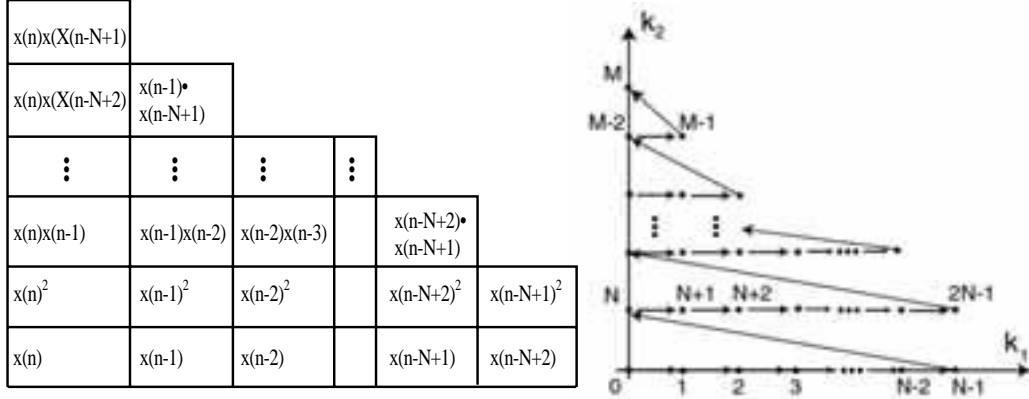


Fig. 1 Input vector restructured into a 2-D input array
 a) ordering scheme for the array b) indexing scheme for the array

when is the memory order of the nonlinear system and $a_{m_1}(n)$ and $b_{m_1,m_2}(n)$ are the linear and quadratic coefficients respectively, of the second order Volterra filter. This expanded input signal vector with nonlinear entries can be restructured into a 2D array as shown in Fig.1. The ordering of the M data points in the support region can be made in various ways. Fig. 1 also shows the indexing arrangement we chose for the input array. It is possible to realize the Volterra system as a joint-process estimator with a lattice-ladder structure instead of the direct form realization as in Eq. 1. Here the lattice section is a 2D lattice predictor for the underlying expanded input signal array with nonlinear entries and the ladder section is a linear combination of the orthogonalized backward prediction errors (Kayran, 1996a, b). In the proposed ordering, we use vertical and horizontal shifts to order the entries within the support into a 1D array. We can observe from the ordering scheme in Fig.1 that the entries exhibit a 1D ordering in the horizontal direction for each row. This ordering was chosen on purpose to eliminate some lattice sections in the full-complexity 2D lattice filter. Using this shift invariance structure along the rows, we can perform the orthogonalization within

each row utilizing the regular 1D FIR lattice filter. The resulting 2D lattice predictor with significantly decreased number of lattice sections is the reduced complexity 2D orthogonal lattice filter.

We use the ladder-section of the joint-process estimator to form an estimate of some primary input using the backward prediction errors. In the system identification mode this input will be the output from a second-order Volterra filter. Fig.2 depicts the nonlinear joint-process estimator, complete with the reduced complexity lattice predictor and ladder section for the case.

II.2 Nonlinear system identification using RLS adaptation

The backward prediction errors $b_0^{(0)}(k_1, k_2), b_1^{(1)}(k_1, k_2), \dots, b_m^{(m)}(k_1, k_2)$ generated using the 2D lattice filter are orthogonal to each other (Kayran, 1996a). This result provides the main advantage of our structure over the multichannel lattice structure in (Syed and Mathews, 1994). For the structure in (Syed and Mathews, 1994), although the backward prediction errors in different channels are orthogonal to each other, the elements within

each channel are not orthogonalized. However, in our structure the backward prediction errors are fully orthogonalized to each other. This will result in faster and less input dependent adaptation in gradient descent type of algorithms such as (normalized) LMS. However, here we develop an RLS-type adaptive algorithm for our novel structure to permit comparison with the algorithms in (Syed and Mathews, 1994).

The orthogonalization within each row of the input array along the horizontal direction utilizes 1D FIR lattice filters. Hence, for the adaptation of the reflection coefficients in each of this 1D lattice filters we used the regular RLS lattice adaptation using a posteriori

estimation errors (Manolakis et al., 2000). This provides for fast, computationally simple and numerically robust adaptation for the 1D lattice sections. For the reflection coefficients in the lattice module sections which provide for the inter-row orthogonalization, the shift invariance is no longer valid. However, the 2D lattice predictor ensures that the backward prediction and forward prediction errors, which are the inputs to the lattice modules are orthogonalized. We can employ this decoupling property of the lattice structure and develop RLS adaptation algorithms for each single lattice stage inside the lattice modules separately. The RLS time update equations for the backward and forward prediction reflection coefficients are given in Table

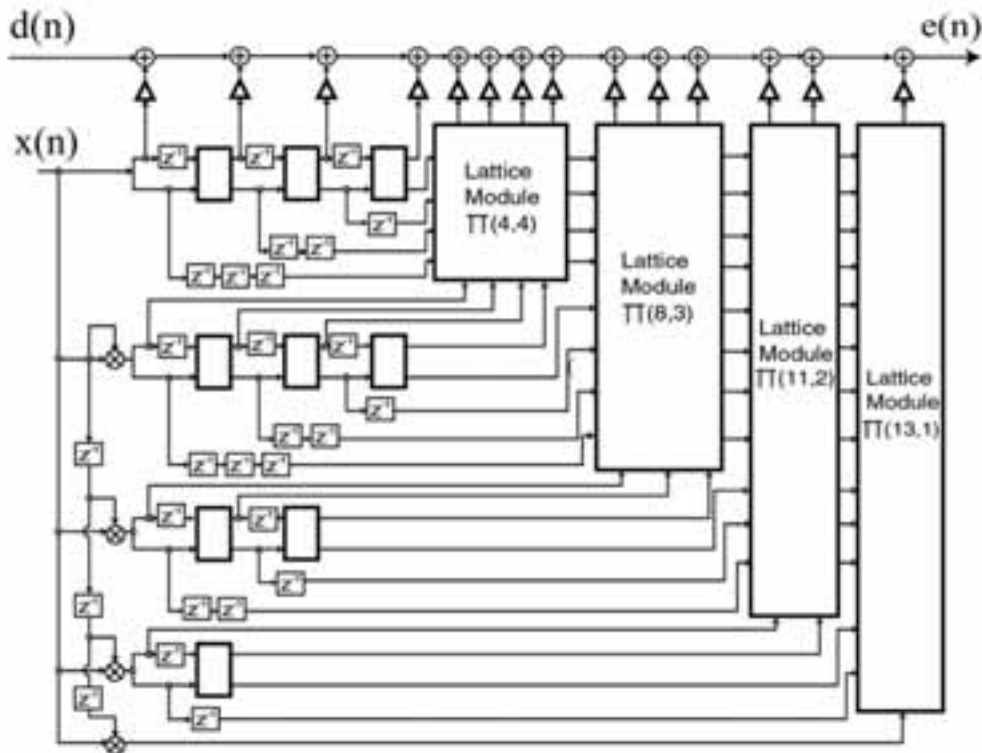


Fig. 2 Nonlinear joint-process estimator for $N = 4$

1 where i is the time index. We set $P(0) = \delta^{-1}$ where δ is a small positive constant and $e(0) = 0$. In Table 1, $\Gamma_{f_{p-n}}^{(n)}$ and $\Gamma_{b_p}^{(n)}$ are the real-valued n^{th} stage reflection coefficients for the forward and backward predictors, respectively (Kayran, 1996a, b). The decoupling property of the lattice filter is also valid for the ladder section. Hence, we use similar update equations for the ladder coefficients.

III. RESULTS AND DISCUSSION

In the simulation the adaptive filter was run with the same structure as that of the second-order Volterra filter to be identified. For the Volterra filter we chose $N=4$, hence the system had 4 linear and 10 quadratic coefficients. The values of the coefficients are taken from system in the example in (Syed and Mathews, 1994) by truncating the system given in (Syed and Mathews, 1994) to $N=4$. The input signal to the unknown system was colored pseudo-Gaussian noise obtained as given in (Syed and Mathews, 1994). The desired response signal $d(n)$ was obtained by adding white Gaussian noise uncorrelated with the input signal. The variance of the observation noise was

chosen to obtain an SNR of 20 dB. We present the learning curves for our lattice structure, the multichannel lattice in (Syed and Mathews, 1994) and the direct form transversal realization (Mathews, 1991) all with RLS adaptation in Fig.3. The error curves are mean squared for 500 cycles and $\lambda=0.9975$. Our structure maintains the excellent numerical behaviour of lattice models and overcomes the deterioration in the convergence speed compared to the transversal RLS filter we observe in the multichannel lattice model, which is due to the increased complexity of this structure (Syed and Mathews, 1994).

IV. CONCLUSIONS

In this letter, a new method is developed for the realization of the second-order Volterra filters utilizing the 2-D orthogonal lattice structure. An RLS adaptive nonlinear filter based on this structure is presented. The performance of our structure in the adaptive system identification setting is superior to previous models (Mathews, 1991), (Syed and Mathews, 1994).

Table 1. Practical implementation of the RLS adaptation algorithm for the reflection coefficients inside the lattice modules.

forward prediction coefficients adaptation	backward prediction coefficients adaptation
$\bar{g} = P_f(i-1)f_{p-n}^{(n-1)}(i)$	$\bar{g} = P_b(i-1)b_p^{(n-1)}(i)$
$\alpha = \lambda + \bar{g}f_{p-n}^{(n-1)}(i)$	$\alpha = \lambda + \bar{g}b_p^{(n-1)}(i)$
$g = \frac{\bar{g}}{\alpha}$	$g = \frac{\bar{g}}{\alpha}$
$P_f(i) = \lambda^{-1}(P_f(i-1) - g\bar{g})$	$P_b(i) = \lambda^{-1}(P_b(i-1) - g\bar{g})$
$e = b_p^{(n-1)}(i) + \Gamma_{f_{p-n}}^n(i-1)f_{p-n}^{(n-1)}(i)$	$e = f_{p-n}^{(n-1)}(i) + \Gamma_{b_p}^n(i-1)b_p^{(n-1)}(i)$
$\Gamma_{f_{p-n}}^n(i) = \Gamma_{f_{p-n}}^n(i-1) + ge$	$\Gamma_{b_p}^n(i) = \Gamma_{b_p}^n(i-1) + ge$

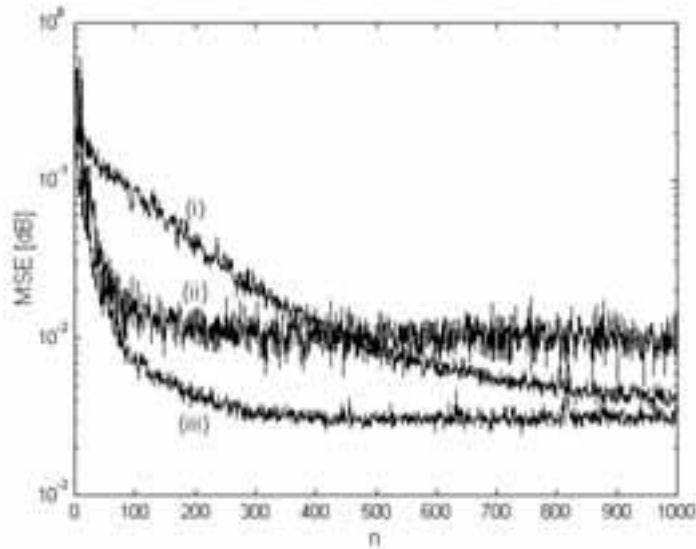


Fig. 3 Learning curves for different models.

- (i) multichannel lattice structure
- (ii) transversal direct-form realization
- (iii) model based on 2-D lattice structure

REFERENCES

- Kayran, A.H., (1996a). Two-dimensional orthogonal lattice structures for autoregressive modeling of random fields, *IEEE Trans. Signal Processing*, vol. 44, No. 4, pp. 963-978.
- Kayran, A.H., (1996b). 2D ARMA lattice modelling using two-channel AR lattice approach, *Electronics Letters*, vol. 32, No. 16, pp.1434-1435.
- Kayran, A.H., (1996c). 2D maximum likelihood spectrum estimation using orthogonal 2D lattice filters, *Electronics Letters*, vol. 32, No. 15, pp.1339-1340.
- Manolakis, D.G., Ingle, V.K., Kogon, S.M., (2000). *Statistical and Adaptive Signal Processing*, Boston.
- Kayran, A.H., Ekşioğlu, E., (2000a). 2D FIR Wiener filter realization using orthogonal lattice structures, *Electronics Letters*, vol. 36, No. 12, pp. 1078-1079.
- Mathews, V.J., (1991). Adaptive polynomial filters, *IEEE Signal Proc. Magazine*, pp. 10-26.
- Syed M.A., Mathews, V.J., (1994). Lattice algorithms for recursive least squares adaptive second-order Volterra filtering, *IEEE Trans. Signal Processing*, vol. 41, No. 3, pp. 202-214.

INSTRUCTIONS TO AUTHORS

Aims and scope

Turkish Journal of Telecommunication (TJT) serves as a forum for the scientific and technical community, working in the fields of telecommunication, information technology, and communication electronics. TJT accepts research articles and short communications in various fields of analog and digital telecommunication, radar, microwave, information technology, and communication electronics. Manuscripts must be based on original research and contain novel findings of general significance. Manuscripts submitted to the TJT must not have been published or be under consideration for publication elsewhere, other than as an abstract of an oral or poster presentation. Manuscripts are welcomed from all countries, but must be in English.

Manuscripts may be rejected without peer review if they do not comply with the instructions to authors or are beyond the scope of the journal. All manuscripts must be accompanied by the Copyright Release form, which can be found in each issue of the journal, or web site www.tk.gov.tr. This form must be completely filled out and signed by corresponding author before processing of the manuscripts can begin.

Submission of manuscripts

Three copies the manuscripts (one is original) printed double-spaced with 3 mm margin on all sides of the page should be submitted to :

Prof. Dr. İnan Güler, Editor-in- Chief,
Turkish Journal of Telecommunication
Telekomünikasyon Kurumu
Yeşilbırmak Sok. No: 16
06430 Maltepe/ ANKARA
Tel : 0312 550 50 37
Fax : 0312 550 52 46
e-mail : iguler@tk.gov.tr
btm@tk.gov.tr

Electronic submission of the manuscripts

Electronic manuscripts have the advantage that there is no need for the rekeying of text, thereby avoiding the possibility of introducing errors and resulting in reliable and fast delivery of proofs. For the initial submission of manuscripts for consideration, hardcopies are sufficient. For the processing of accepted papers, electronic versions are preferred. After final acceptance, your disk plus three final and exactly matching printed versions should be submitted together. On the other hand, authors can directly submit

their manuscript via e-mail. Word files may be sent via e-mail (iguler@tk.gov.tr) or FTP. Submission as an e-mail attachment is acceptable provided that all files are included in a single archive the size of which does not exceed 2 megabytes. Larger files (e.g., those with large images) should be submitted to the FTP site. Authors are requested to include in their electronic submission a cover letter and all ancillary materials. All file names should include the corresponding author's last name.

Preparation of manuscripts

Manuscripts should follow this order: Title Page, Abstract with title of manuscripts and names of authors. Özet (Turkish Abstract), Introduction, Materials and Methods, Results, Discussion, Acknowledgements (if necessary) and References. When the Results and Discussion sections are combined, then a Conclusions section should be added. The total number of double-spaced pages of the Abstracts, Introduction, Materials and Methods, Results and Discussion must not exceed 15 for regular articles and 6 for short communications. Section and sub-section heading should not be numbered.

Title Page: The first page should contain a concise and informative title not exceeding 15 words, the names and addresses of the authors and contact details of the corresponding author (postal address, e-mail, and fax and telephone numbers).

Abstract: The abstract must be in both English and Turkish, and should not exceed 200 words for the English 500 words for the Turkish abstract. In the case of short communications, abstract should not contain more than 100 words. The Abstract should be informative as to why and how the study was conducted, and what the results and conclusions were. Editorial office can provide Turkish abstract for the authors whose native languages are not Turkish.

A maximum of 6 key words must be given at the end of the Abstract, allowing a one-line space.

Introduction: This part should define the background and significance of the problem by considering the relevant literature, particularly the most recent publications. The reasons why the study was conducted must be mentioned in this section.
Materials and Methods: Please provide concise but complete information about the materials and methodological procedures used. This part should be as possible to enable other scientists to repeat the research presented.

Results: In this part, the same data/information given in a table must not be repeated in a figure, or vice-versa. It is not acceptable to repeat extensively the numbers from Tables in the text and give long explanations of the tables and Figures.

Discussion: This part must be written with reference to the tables and figures and by considering information from the literature.

Statements made in the Introduction and Results sections should not be repeated here.

Acknowledgements: If necessary, a brief Acknowledgements section may be included.

References: References should be cited in the text by the last name(s) of the author(s) and year of publication, for example, (Kuntman, 2002) or (Sankur and Kalyoncu, 1992). If the citation is the sentence, then only the date should be given in parentheses, for example, according to Kuntman (2002) or as suggested by Sankur and Kalyoncu (1992). For citation of references with three or more authors, only the first author's name followed by "et al." should be used, for example, (Toker et al., 2002) or as shown by Toker et al. (2002). If there is more than one reference in the same year for the same author(s), then please add the letters "a", "b", etc. to the year, for example, (Kayran, 2001a, b) or (Kayran, 2001a, b, c). Only published papers or papers in press can be mentioned in the manuscript. Papers in preparation or in review can be mentioned within the text as unpublished data, and should not be included in the References section. References should be listed alphabetically at the end of the text without numbering. References should be listed as given below.

Çiçekoğlu, O., N. Tarım, H. Kuntman, (2002). Wide dynamic range high output impedance current-mode multifunction filters with dual-output current conveyors providing wide dynamic range, *International Journal of Electronics and Communications*, 56, 1, pp.55-60.

Kayran, A.H., (1996). Two dimensional orthogonal lattice structures for autoregressive modeling of random fields, *IEEE Transactions on Signal Processing*, 44, 4, pp. 2092-2098.

Couch, L.W., (1990). Digital and Analog Communication Systems, MacMillan, New York.

Patterson, D.A., J.L. Hennessy, (1997). Computer Organization and Design, Morgan Kaufmann, California.

Eroğlu, C.E., B. Sankur, (2000). Performance evaluation metrics for object-based video segmentation, *Proc. 10th European Signal Processing Conference*, pp.917-920, Tampere, Finland.

Burg, J.P., (1975). Maximum Entropy Spectral Analysis, *Ph.Dissertation*, Stanford University, California, p.57, 1975.

Abbreviations: All non-standard abbreviations should be grouped into an abbreviations list and given at the bottom of the first page

of text, allowing a 2-line space.

Figures: Photos or drawing must have a good contrast of dark and light. Legends of figures should be brief, but complete and self-explanatory so that the reader can easily understand the result presented in the figure. Figure legends should not be attached to the figures and should be supplied on a separate page double-spaced. Each figure must be clearly marked on the back with authors' names and figure number. Please do not duplicate material that is already presented in the tables. Dimensions of figures must be maximum 16x 20 cm and minimum 8x20 cm. Tables: Each table must be given on a spare page with a brief but complete and self-explanatory caption so that the reader can easily understand the results presented in the table. Please do not duplicate material that is already presented in the figures. Dimensions of tables must be maximum 16x 20 cm and minimum 8x20 cm.

Final Check List

Before submitting your paper, please make sure that is in the correct format and that the following requirements have all been met:

- Copyright Release form is enclosed, completed and signed by corresponding author
- Paper is submitted in triplicate (one original, 2 copies)
- Entire paper is double-spaced (NOT 1.5) including abstract, tables, captions/legends, references
- Margins are 3 cm each side
- Font size 12 pt. Or 3 mm
- Font is legible
- Names of authors are written in full (not abbreviated)
- English address of authors is given
- Turkish title and abstract are given for Turkish contributors
- Original figures are enclosed
- Figures are prepared according to instructions
- Figures are min. 8x20 cm; min. 16x 20 cm.
- Figures are referred to consecutively in the paper
- Tables are min. 8x20 cm; min. 16x 20 cm.
- Tables are referred to consecutively in the paper
- Table and figure legends captions are typed on separate sheets
- References are cited and listed according to instructions and not numbered.
- The total number of double-space pages of the Abstracts, Introduction, Materials and Methods, Result and Discussion must not exceed 15 for regular articles and 6 for short communications.
- Section and sub-section headings should not be numbered.
- Decimal fractions are indicated by decimal points and commas throughout the paper (e.g., 10.24 NOT 10,24)

TURKISH JOURNAL OF TELECOMMUNICATIONS

Ionospheric Clutter Effects On Monostatic HF Surface Wave
Radar Systems And Clutter Mitigation Techniques

B. Ően, B. Polat

Determining Antenna Factors For EMC Measurements

B. Tretken, A.İ. Yrekli, M. Yazıcı

Segmentation Of Remote-Sensing Images
By The Grow And Learn Network

T. Őlmez, Z. Dokur

Monitoring Urban Changes In Istanbul Province
Between 1992-1995 Using ERS-1 Sar Satellite Images

E. Alparslan

Effects Of The Collisions On The Phase And Group Velocities
Of HF Waves Propagating In The Ionosphere Around Reflection Points

M. Aydođdu, E. Gzel, A. YeŐil

Real Time Computation For Bistatic Sar Imagery

M. Kartal, S. Kent

Novel T/R Antenna Designs For Surface Wave HF Radar Systems
With Narrow Elevation And Azimuthal Beamwidths

A. S. Trk, B. Polat

Adaptive Volterra Filtering Using Complete Lattice
Orthogonalization

E. M. EkŐiođlu, A. H. Kayran